Journal of Materials Processing Tech. 333 (2024) 118614

Contents lists available at ScienceDirect

Journal of Materials Processing Tech.

journal homepage: www.elsevier.com/locate/jmatprotec

Research article

Mechanisms in the machinability improvement of Inconel 718 superalloy through ultra-high-speed grinding

Hao Liu, Huili Han, Qinghong Jiang, Bi Zhang *

Department of Mechanical and Energy Engineering, Southern University of Science and Technology, Shenzhen 518055, China

ARTICLE INFO

Keywords:
Ultra-high-speed grinding
Removal mechanisms
Machinability
Surface integrity
IN718 superalloy

ABSTRACT

Inconel 718 (IN718) superalloy is a typical difficult-to-machine material characterized by low thermal conductivity and severe work hardening. Ultra-high-speed machining (UHSM) exhibits characteristics of material embrittlement and the skin effect of machining damage, which may address the above dual machining issues. This paper investigates the speed effect on the formation of machined surface and, for the first time, achieves ultra-high-speed grinding of IN718 superalloy at a speed up to 240 m/s. The grinding forces and surface integrity across various speed ranges are examined in detail. Multiple techniques are employed to characterize and analyze the subsurface microstructure. The results demonstrate that brittle-mode removal of IN718 superalloy occurs at a grinding speed exceeding 190 m/s, effectively mitigating work hardening and heat generation resulting from intensified plastic deformation. Furthermore, the machining speed influences the formation mechanism of recrystallization layer, gradually transitioning from discontinuous dynamic recrystallization (dDRX) domination to continuous dynamic recrystallization (cDRX) domination with an increase in grinding speed. Meanwhile, multifold nano-twins with a wide range of 4–5 nm form within tens of nanometer grains under UHSM conditions, further altering the subsurface microstructure. These findings provide valuable scientific insights for enhancing the machinability of other difficult-to-machine materials.

1. Introduction

IN718 superalloy exhibits outstanding mechanical, chemical, and thermal properties, including high-temperature strength, thermal stability, corrosion resistance, fatigue resistance, and radiation resistance [1]. It finds extensive applications in extreme environments across various industries, such as aerospace, automotive, marine, petrochemical, and nuclear energy [2]. These attributes also pose challenges for machining, resulting in a notable decrease in the machinability index of IN718 superalloy [3].

One of the challenges in machining IN718 superalloy is its extremely low thermal conductivity. Cryogenic machining effectively responds to the above challenge, which utilizes liquid nitrogen and carbon dioxide to control the machining temperature [4,5], avoiding workpiece burn and minimizing tool wear [6]. High-pressure jet assisted machining significantly boosts the convective heat transfer coefficient [7], through enhancing coolant diffusion [8]. In addition, thermal conductive coating also plays a positive role in making up for the problem of low conductivity [9]. However, compared to methods like using cryogenic coolant and thermal conductive coating during machining, suppressing heat generation at the source is more advantageous for extending tool life and enhancing the continuity of machining [10]. Various methods have been developed to suppress the heat generated during machining from the perspective of minimizing external friction. Minimum Quantity Lubrication (MQL) is a typical method through creating dense lubricant films on the tool-workpiece and tool-chip surfaces. To improve the lubrication performance, solid lubricant-assisted MQL [11] and nanofluid-assisted MQL [12] have been introduced. However, as external frictional heat constitutes only about 25 % of the total heat generated in machining, setting the upper limit on the effectiveness of MQL.

The challenge in machining IN718 superalloy also manifests in work hardening. Laser-assisted [13] and plasma-assisted [14] machining are effective techniques to mitigate work hardening. By preheating with laser or plasma along the machining path, the material of the workpiece is softened beforehand, effectively reducing the hardness and alleviating work hardening. However, the thermal effect from the softening process can lead to negative consequences. Processes such as ablation, melting, and re-solidification introduce thermal stress into the material of the

* Corresponding author.
E-mail addresses: 12131088@mail.sustech.edu.cn (H. Liu), 11930603@mail.sustech.edu.cn (H. Han), 11968003@mail.sustech.edu.cn (Q. Jiang), zhangb@sustech.edu.cn (B. Zhang).

https://doi.org/10.1016/j.jmatprotec.2024.118614
Received 13 September 2024; Accepted 24 September 2024
Available online 25 September 2024

machining area, significantly increasing the risk of crack formation.

Based on the above analysis, auxiliary processes are commonly employed to enhance the machinability of IN718 superalloy. However, the addition of lubrication, cooling and preheating devices increases the complexity of the production process and the uncertainty of industrial control, which is not conducive to the economy and green sustainability. Meanwhile, these methods are usually attended to one thing and lose sight of another, cannot overcome the above dual machining challenges of IN718 superalloy simultaneously, so the improvement of its machinability has not reached the ideal expectations. Therefore, developing a high-quality, high-efficiency, low-damage, and low-cost machining method is crucial to address the dual challenges of low thermal conductivity and work hardening. Ultra-high-speed machining (UHSM), characterized by material embrittlement [15] and the skin effect of machining damage [16], emerges as the preferred solution.

In this paper, machining that exceeds the critical speed of ductile-brittle transition of the material is defined as UHSM [17], and machining speed that falls between conventional and ultra-high speeds is defined as high-speed machining. The critical speed of the ductile-brittle transition depends on the material's physical and mechanical properties, loading strain rate, and is directly associated with the material's strain rate sensitivity [15], machining environment, and the machining speed and depth [18]. In recent years, UHSM has been facilitated by equipping machine tools with ultra-high-speed spindles and modifying devices such as a Hopkinson pressure bar. During UHSM, the extremely short contact time between the tool and the workpiece, along with rapid stress release, leads to unique material removal mechanisms unlike those in conventional and high-speed machining. Eda et al. [17] initially proposed that when cutting speeds surpass the static plastic wave propagation speed, plastic deformation on the surface layer of the workpiece material is significantly suppressed. Zhou et al. [19] conducted ultra-high-speed grinding tests on pure aluminum A1199 and aluminum alloy A5056, noting that high strain rates can narrow the gap between the yield and ultimate strengths of the workpiece material. As the yield and ultimate strengths converge, the material removal transitions from ductile to brittle, exhibiting no significant plastic flow in the subsurface of the workpiece. Liu et al. [20] conducted ultra-high-speed cutting experiments on AerMet100 steel, further confirming the brittle-mode removal via the non-plastic, granular chips. Yang and Zhang [15] pointed out that material embrittlement under high strain rates is a temporary state, and the material recovers its original plasticity after machining, introducing the concept of pseudo-embrittlement. Wang et al. [21] conducted ultra-high-speed cutting experiments on IN718 superalloy and 7050-T7451 aluminum alloy, and observed distinct brittle cracks and cleavage steps in the chips, confirming that brittle-mode removal under the ultra-high-speed condition also applies to IN718 superalloy. Guo et al. [22] explored the material removal mechanism of Al/SiCp composite materials in ultra-high-speed grinding, concluding that UHSM can reduce the property discrepancies between the aluminum alloy matrix and SiC particles, thereby enhancing the surface integrity. To address the issue of poor surface integrity in titanium alloys prepared by selective laser melting, Jiang et al. [23] employed single-point scratching experiments to reveal the deformation mechanism of this material under extremely high strain rates, providing a viable solution for efficient post-machining in additive manufacturing. Ueda et al. [24] discovered that the heat transferred into the chips increased with an increase in machining speed, while the workpiece and tool were not significantly affected by the cutting heat. The aforementioned studies demonstrate that UHSM has great potential in solving the machinability issues.

However, previous studies primarily concentrated on the feasibility and critical conditions for brittle-mode removal in ductile materials, and did not delve into the brittle-mode removal mechanisms under UHSM from the perspective of machinability for hard-to-machine materials. Moreover, to the authors' knowledge, the current maximum machining speed for IN718 superalloy is 133 m/s, and the material removal mechanisms at higher speeds require further exploration. Unlike continuous machining methods such as cutting, the grinding process involves the combined action of different abrasive grains. Intermittent removal by the same grain effectively controls tool wear and excessive machining temperature, making grinding as the preferred method for UHSM [25]. Therefore, this paper conducted grinding experiments at speeds ranging from 20 to 240 m/s, comprehensively assessing the machinability of IN718 superalloy in terms of force, temperature, surface quality, subsurface damage, and work hardening. It also summarizes the microstructure evolution and response mechanisms at different grinding speeds and elucidates the material removal mechanisms for UHSM IN718 superalloy.

2. Material and experimental procedures

2.1. Workpiece material

The workpiece material for this grinding experiment was a rolled plate of IN718 superalloy treated by solution annealing (complying with ASTM B670). Its chemical composition and primary physical-mechanical properties are detailed in Tables 1 and 2 [26]. Fig. 1a illustrates the internal grain size distribution of the material, with grain diameters mostly ranging from 15 to 38 μm and an average size of 21.3 μm. The inset depicts a random distribution of grain orientations and a notable presence of annealing twins. Fig. 1b further shows the microstructure of IN718 superalloy. Dense wheat-shape grains δ phase (Ni_3Nb) are uniformly distributed on the grain boundaries, which together with a small number of carbo-nitrides constitute the main phases of this material. Meanwhile, there is also a minor amount of undissolved white Laves phase. In addition, since the workpiece was not subjected to age-hardening, no precipitate-hardened γ' and γ'' phases were observed within the grains.

2.2. Grinding setup and experimental procedures

As shown in Fig. 2, this experiment was conducted on a high-speed grinder (Hardinge GT27), outfitted with a hydrostatic spindle manufactured by the Swiss company TDM, capable of reaching a maximum rotation speed of 60,000 rpm. The IN718 superalloy plate was machined into 10 × 10 × 3.5 mm workpieces using a wire electrical discharge machine (Sodick AG400L). These workpieces were then clamped to the work spindle with a steel disc measuring 190 mm in diameter and 8 mm in thickness. The workpieces were affixed to the disc with strong AB adhesive, and the bond strength was evaluated using a 1 kg hanging weight. During the UHSM process, the extremely high linear speeds imposed greater demands on the strength of the grinding wheel. A ceramic-based CBN superabrasive wheel was employed in the experiment, and high-strength, low-density carbon fiber-reinforced plastic (CFRP) was utilized as the matrix to reduce rotational inertia at ultra-high speeds, with specific parameters detailed in Table 3.

Before each grinding experiment, the CBN grinding wheel was dressed with a diamond roller and sharpened using a SiC wheel, followed by pre-grinding the workpiece with fixed parameters to ensure that the abrasive particles entered a stable working state and the workpiece surface to be ground was fully in contact with the grinding wheel. Subsequently, dynamic balancing tests and adjustments were carried out on the grinding wheel using a dynamic balancer (BMT240M.2), limiting the imbalance of the wheel to within 10 mg at the grinding speed. This was to ensure smooth operation of the grinding wheel under ultra-high-speed conditions and the safe conduct of the experiments. As detailed in Table 4, the grinding test was segmented into eight groups, employing an up-grinding method, where both the grinding wheel and workpiece axes rotated counterclockwise (opposite rotational directions in the grinding zone). The actual grinding speed v_g is the sum of the grinding wheel's linear speed v_s and the workpiece's linear speed v_w, reaching up to 240 m/s. During the grinding process, a

Table 1
Chemical compositions of IN718 superalloy (wt%).

Element	Ni	Cr	Fe	Mo	Cu	Al	Ti	Nb	C
Min.(%)	50	17	-	2.80	-	0.20	0.65	4.75	-
Max.(%)	55	21	Bal.	3.30	0.30	0.80	1.15	5.50	0.08

Table 2
Physical and mechanical properties of IN718 superalloy.

Thermal conductivity (W/m·k)	Specific heat capacity (J/Kg·K)	Tensile strength (MPa)	Yield strength (MPa)	Modulus of elasticity (GPa)	Poisson's ratio	Density (g/cm^3)
14.70	435	965	550	199.90	0.30	8.24

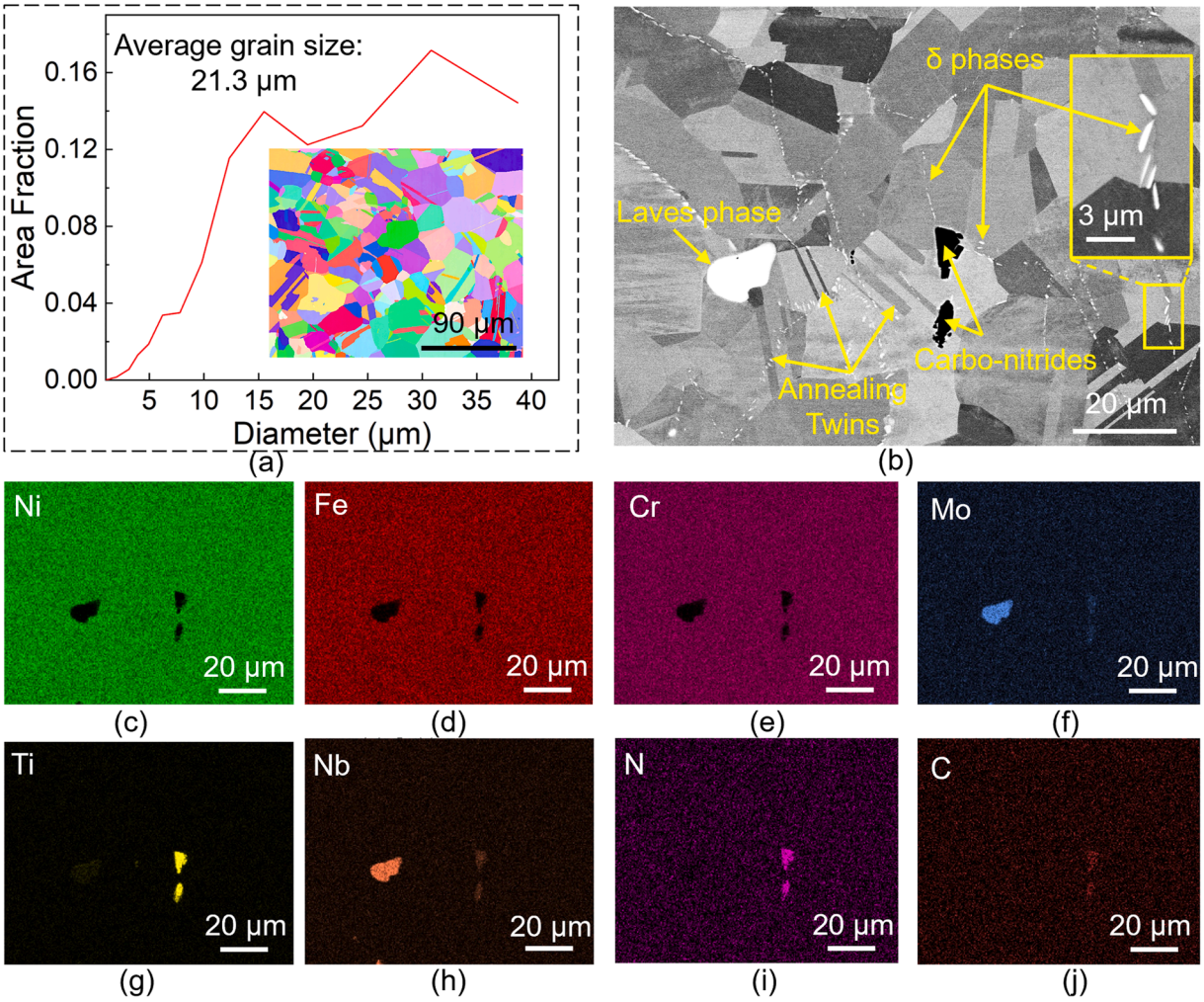

Fig. 1. Microstructure of IN718 superalloy. (a) Size distribution of the grain, (b) microstructure of IN718 superalloy, and (c-j) the element distributions of (b).

water-based coolant was employed at a flow rate of 10 L/min. The total grinding depth for each group was set at 500 μm to negate any impact from pre-grinding parameters on the workpiece.

2.3. Measurement and characterization methods

Surface morphology of the machined workpiece was examined using secondary electron mode of a scanning electron microscope (FEI Apreo 2 S). Surface roughness and microhardness values were measured respectively using a non-contact optical 3D profilometer (Taylor Hobson CCI HD) and a microhardness tester (HXD-1000TMC/LCD), applying a 500 g load and a 10-second hold time for the latter. After calculation, the indentation depth is about 5.7 μm, which is smaller than the deformation layer thickness of all machined samples. Phase composition and lattice constant variations of the workpiece were analyzed using an X-ray diffractometer (XRD, Rigaku Smartlab), setting the X-ray wavelength at 1.54178 Å. According to the measured material, X-ray incidence angle and the selected target material, it is determined that the X-ray penetration depth is within the range of 10–20 μm, which meets the measurement requirements of the machining deformation area. Subsurface microstructural morphology was characterized using the electron back-scattered diffraction (EBSD) technique of the scanning

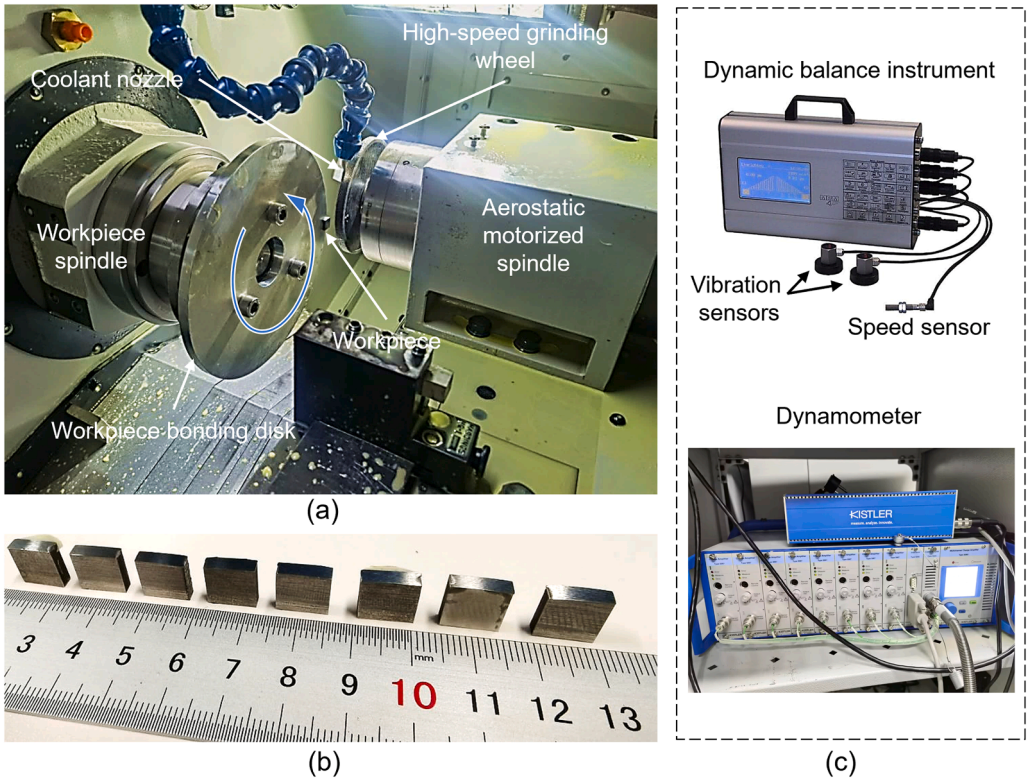

Fig. 2. (a) Grinding setup for cylindrical grinding IN718 superalloy, (b) ground workpieces, and (c) auxiliary monitoring devices.

Table 3
Parameters of the grinding wheel.

Abrasive layer (mm)	Substrate	Mesh size	Concentration	Overall size (mm)
Ceramic bond CBN (4×8)	CFRP	80/100#	175 %	118×10×15

Table 4
Experimental scheme for cylindrical grinding IN718 superalloy.

Groups	ν_s (m/s)	ν_w (m/s)	ν_g (m/s)	a_p (μm)	f (mm/min)
1	20	20	40	5	150
2	50		70		
3	80		100		
4	110		130		
5	140		160		
6	170		190		
7	200		220		
8	220		240		

electron microscope, with a scan step size uniformly set at 0.3 μm. Prior to the EBSD scan, the workpiece cross-section perpendicular to the grinding surface was prepared using SiC sandpaper with 600#, 1000#, 2000#, and 3000#, followed by three hours of vibrational polishing with SiO_2 polishing liquid to eliminate stress and enhance the indexing rate. Additionally, to examine the internal nanostructure of recrystallized layer, observation samples were prepared using a focused ion beam system (Helios 600i), as depicted in Fig. 3. Initially, a Pt protective layer was deposited along the grinding direction at the selected observation site. This was followed by creating big pits and a "U" cut to extract the sample. Finally, both sides were uniformly thinned to prepare the sample of about 100 nm thickness. Transmission electron microscopy (Talos F200X G2) was employed to observe the nanostructure with an acceleration voltage of 200 kV. Meanwhile, transmission Kikuchi diffraction (TKD) technique was utilized to calibrate information on nanocrystals in the recrystallized layer, with a uniform scanning step of 5 nm, and setting scanning voltage and current to 30 kV and 6.4 nA, respectively.

To ascertain the trend of grinding force in relation to grinding speed, a dynamometer (KISTLER 5080 A) was employed to measure the grinding force, with a sampling rate of 2000 Hz. Data was finalized after filtering and zero-point compensation operations. Notably, the workpiece axis remained fixed during force measurement. To maintain a consistent material removal rate, the feed rate was set at a fixed ratio to the grinding speed.

3. Results and analysis

3.1. Machined surface morphology and mechanical properties

Fig. 4 depicts the surface morphology of grinding at different linear speeds, where (a)-(d) correspond to the overall morphology at speeds of 40, 100, 160, and 220 m/s, respectively. It is evident that increasing grinding speeds shows a marked improvement in the overall surface finish. Fig. 4e-h shows zoomed-in views at corresponding speeds. At 40 m/s, severe material smearing on the surface occurs, with smearing particles ranging in size from 2 to 8 μm and associated with notable ductile tearing. At 100 m/s, the surface smearing is somewhat reduced, showing side flow and adhesion layer, indicating increased plastic flow of material. With further increases in grinding speed, the size and impact range of the smearing particles are greatly reduced, almost completely suppressed at 220 m/s. It is worth pointing out that, as shown in Fig. 4h at 220 m/s, localized recasting layers and high-density pores appear, both on a sub-micron scale. Additionally, influenced by the hard phases in the matrix, cracks occur at these phases at different grinding speeds (as shown in Fig. 4f).

Fig. 5 displays the surface roughness at varying grinding speeds, demonstrating a trend where roughness decreases initially and then increases. At a conventional grinding speed of 40 m/s, the surface finish

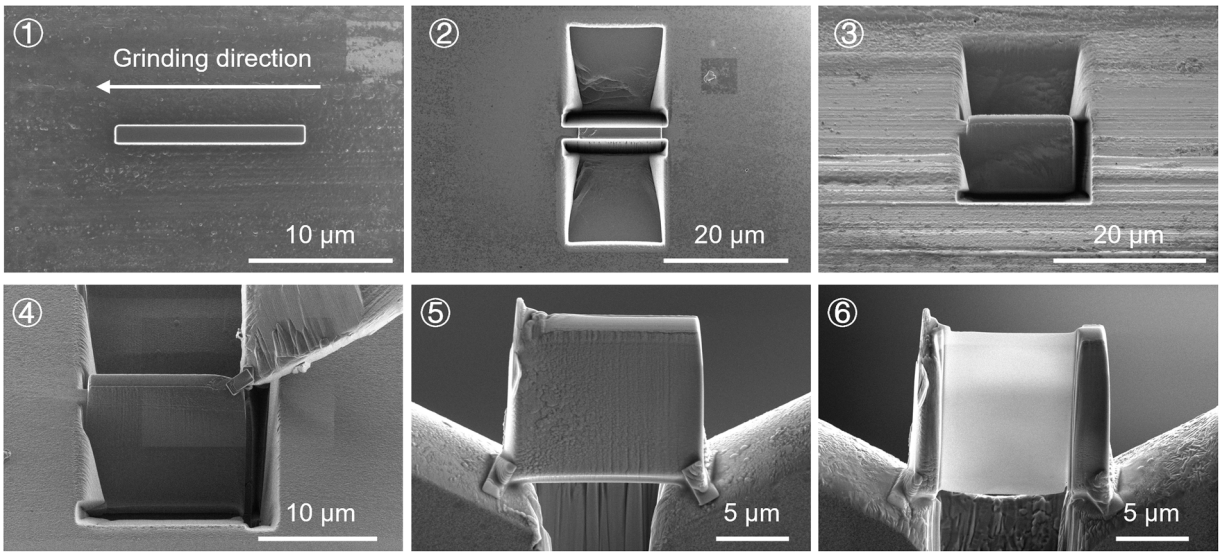

Fig. 3. The specific process of preparing transmission sample.

is the poorest, exhibiting an average roughness of 0.3 μm due to material smearing and ductile tearing. Within the high-speed grinding range of 100–160 m/s, the roughness gradually decreases to its minimum. As grinding speeds continue to increase, the strain rate effect dominates, and surface material becomes more brittle as material embrittlement during grinding progress. Material embrittlement leads to poor elastic recovery ability of materials after grinding, resulting in deeper grinding marks and a slight rise in roughness. Fig. 6 illustrates the trend in surface microhardness after grinding, noting that unmachined IN718 superalloy has a microhardness of 290 HV. Test points are on the machined surface. There is significant work hardening after grinding, with the overall microhardness ranging from 400 to 500 HV. Microhardness values initially increase with grinding speed, peaking at 485 HV at 100 m/s. Further increases in grinding speed effectively mitigate the work hardening of IN718 superalloy, with microhardness under ultra-high-speed conditions (220–240 m/s) at 425 HV, representing an overall reduction of 20.69 % relative to the material as received.

To investigate the occurrence of phase transformation, XRD analyses were conducted on ground surfaces at different linear speeds, as shown in Fig. 7. Fig. 7a shows the diffraction peaks at various grinding speeds, with unmachined workpieces predominantly comprising γ and δ phases. After grinding, there was a significant reduction in the intensity of diffraction peak, and the γ(400) peak disappeared, with no evident phase transformation detected. However, the force-heat coupling effect at different grinding speeds caused varying degrees of lattice distortion. Fig. 7b, c provides magnified views of the γ(111) and γ(200) peaks at various speeds. It can be observed that compared with the unmachined workpiece's central peak line, the shift angle of the peak first increases and then decreases with increasing grinding speed, and the maximum deviation occurs within the 100–130 m/s speed range. According to Bragg's equation, a leftward shift in the face-centered cubic lattice suggests an increase in lattice constants, indicating more severe plastic deformation at speeds of 100–130 m/s, while at ultra-high speeds of 220–240 m/s, the surface plastic deformation is minimal.

3.2. Grinding force

Fig. 8a-h displays the grinding force measurement at various speeds, where red and blue lines represent the grinding forces in the feed and grinding direction, respectively. Notably, the grinding force fluctuates significantly in the 100–130 m/s speed range, whereas it is relatively stable at other speeds. Fig. 8i shows the overall trend of grinding force across different speeds, fitted with a polynomial curve (correlation coefficient R-square $>$ 0.99). Initially, the total grinding force (black line) increases to a maximum of 1.02 N within the 20–70 m/s speed range. As speed rises beyond this range, the force gradually decreases, reaching 0.36 N at 160 m/s, and gradually stabilizes beyond 160 m/s. It is noteworthy that the grinding force at speeds above 160 m/s is comparable to that at 20 m/s. Based on the overall trend of grinding forces, the grinding speed range can be divided into several zones: ductile-mode removal zone (work hardening zone and temperature softening zone), ductile-to-brittle transition zone, and brittle-mode removal zone, which can be further validated by subsequent analysis.

3.3. Subsurface damage

Fig. 9a-h shows the subsurface inverse pole figure (IPF) plus image quality (IQ) maps at different grinding speeds, along with the trend (i) of the white layer plus severe deformation area depth (WPSD) beneath the surface, with the legend indicating different crystal orientation. It is evident that beneath the ground surface, there are I-white layer, II-severe deformation area and III-bulk material. At conventional grinding speeds of 40–70 m/s, the severe deformation area exhibits clear signs of plastic flow, with grains elongated and aligned with the grinding direction, as indicated by the white slip lines in Fig. 9a, b. The WPSD ranges from 20 to 24 μm within this speed range. As grinding speed increases, the extent of these two layers gradually reduces. In the high-speed grinding range of 130–190 m/s, the WPSD is within 16–20 μm, showing relatively minor change. At ultra-high speeds of 220–240 m/s, the WPSD is confined to within 10 μm, approximately a 50 % reduction in depth compared to conventional grinding, and there are no significant traces of plastic flow.

Fig. 10a-h illustrates the subsurface kernel average misorientation (KAM) maps at varying grinding speeds and the depth trend of grains undergoing orientation change (i), where the legend shows a color gradient from dark blue to red, indicating increasing misorientation. The bulk material shows dark blue as it is unaffected by the grinding process; however, at the grain boundaries, due to residual stresses from the recasting process, a faint green is observed, but the color becomes more intense and concentrated due to misorientation caused by grinding, these two showing a clear distinction. In addition, some defects introduced during the material preparation can also cause misorientation, and these effects can be isolated using the microstructure details in the IPF+IQ maps, as marked in Fig. 9. Closer to the ground surface, the color transitions from grass green to dark yellow, signifying severe grain deformation in the shallow layer where stress is the most concentrated.

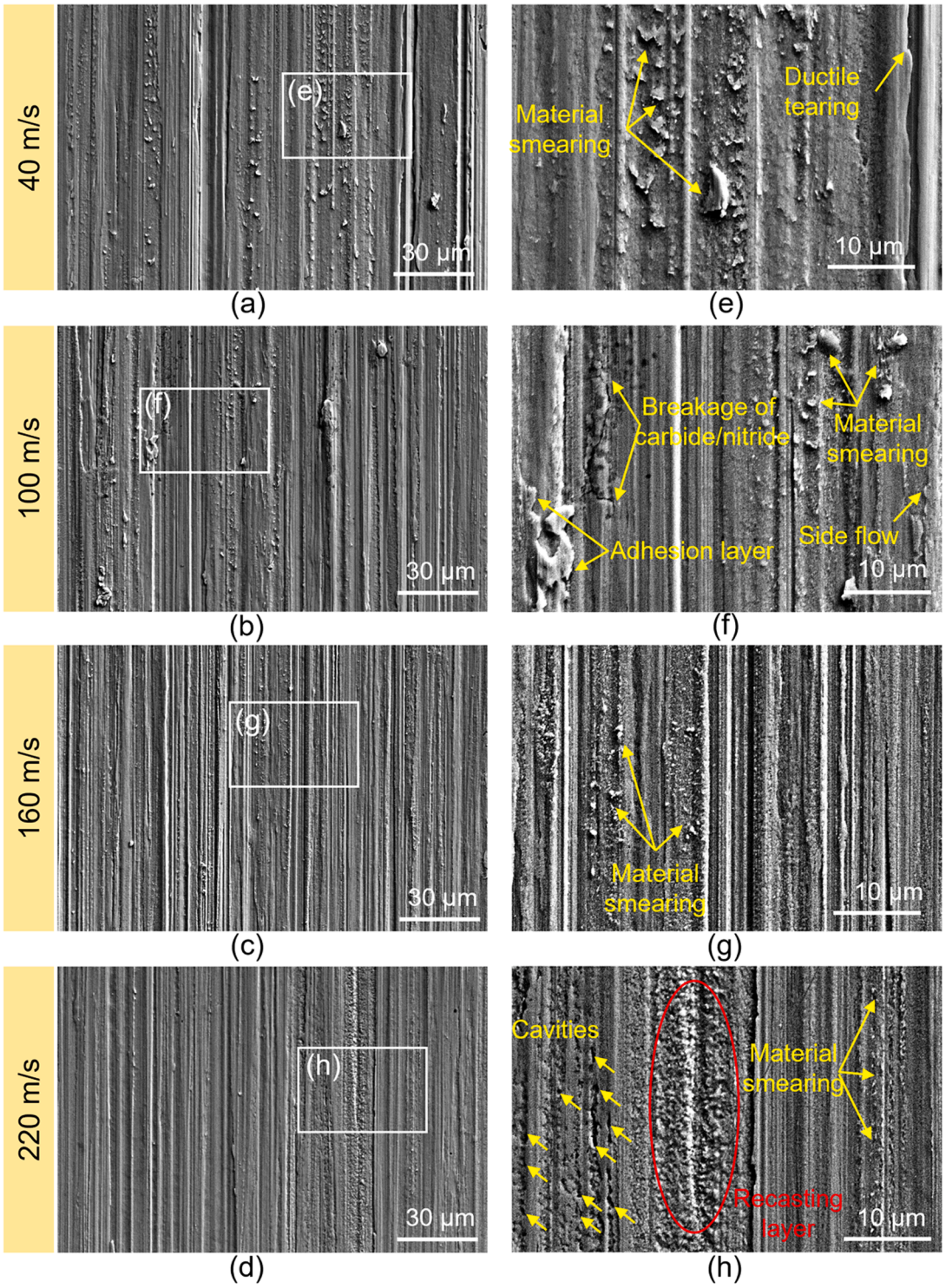

Fig. 4. The topography of ground surface at different linear speeds. (a) 40 m/s, (b) 100 m/s, (c) 160 m/s, and (d) 220 m/s; (e), (f), (g) and (h) are the corresponding enlarged images.

Interestingly, the variation trend of the misorientation radiation range does not match that of the WPSD. It first increases and then decreases with grinding speed, reaching its maximum extent of about 120 μm within the high-speed grinding range of 100–160 m/s. Particularly, at grinding speeds of 100 and 130 m/s, significant strain concentration persists in areas remote from the ground surface. In comparison, the influence is confined to within 40 μm at ultra-high speeds of 220–240 m/s. The reason of different trend is that the white layer and severe deformation area, responsible for severe grain deformation, is heavily influenced by grinding forces. The KAM maps also reflect minor deformation, including the impact of thermal stress, especially at places far away from the ground surface.

3.4. *Subsurface microstructure evolution*

Subsurface damage significantly affects the lifespan of machined components, emphasizing the need for a thorough understanding of the speed effect on the microstructural evolution mechanisms, especially of

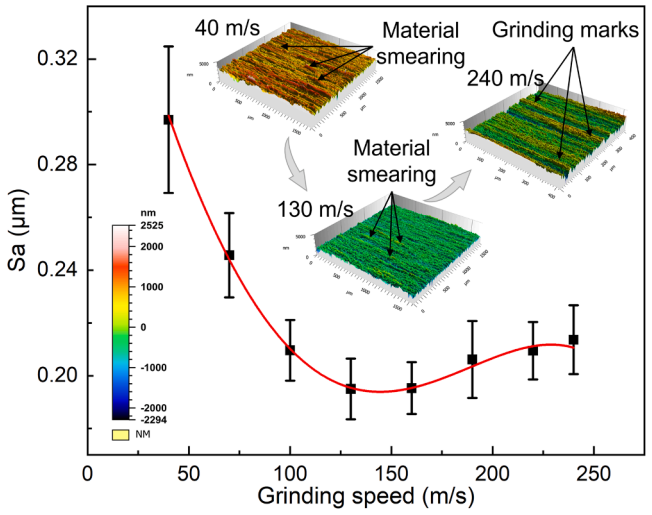

Fig. 5. The variation of surface roughness with grinding speed.

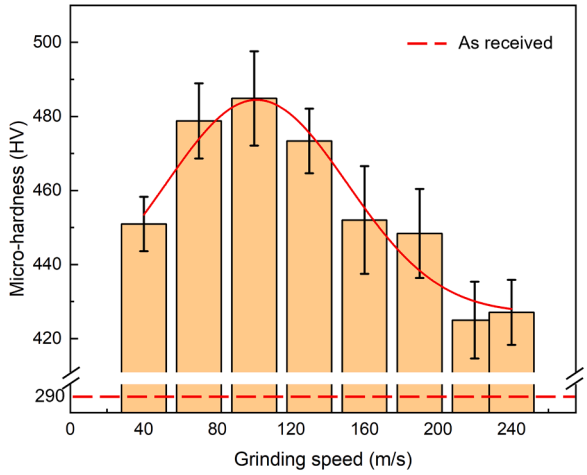

Fig. 6. The variation of Micro-hardness with grinding speed.

the recrystallized layer. Fig. 11 illustrates the microstructural morphology of the unmachined workpiece's subsurface, featuring complete grains with clear grain boundaries. Influenced by the sample preparation process, the first grain contains a few dislocation lines, as shown in Fig. 11b. Additionally, the δ strengthening phase is regularly aligned along the grain boundaries. Fig. 12 presents the microstructural morphology of the subsurface at a conventional grinding speed of 40 m/s, which primarily includes grain refinement layer, transition layer, and plastic flow layer. The grain refinement layer has an average depth of 1.68 μm, resulting from recrystallization during grinding. Electron diffraction reveals rings corresponding to various crystal orientations, as illustrated in Fig. 12b. Fig. 12c further illustrates the microstructure of the grain refinement layer, consisting mostly of equiaxed nanocrystals ranging from 20 to 100 nm. High-resolution magnification image in Fig. 12e reveals slight lattice distortions within the recrystallized grains, and there is no significant dislocation formation, indicating mild surface plastic deformation at this speed. The inner lattice of the recrystallized grains undergoes an inverse Fourier transform to generate electron diffraction spots, depicted in Fig. 12f, aligning with the selected area electron diffraction results in Fig. 12g, all along the $[\bar{1}12]$ crystallographic zone axis without twinning existence. The transition layer extends to a depth of about 5.31 μm, as shown in Fig. 12d, with grains elongated nearly horizontally and encircled by a high density of dislocations. The transition layer is also a recrystallized layer but that is not completely transformed, and therefore consists of low-angle grains and subgrains [27], resulting from the decrease of thermal and strain energy from the ground surface to the bulk material. In addition, the plastic flow layer comprises numerous micrometer-scale twins within the grains, which will be detailed in subsequent content.

Fig. 13 displays the microstructural morphology of the workpiece's subsurface at a grinding speed of 160 m/s. With increased grinding speed, the average depth of the grain refinement layer decreases to 1.25 μm and that of the transition layer to 3.01 μm, with their boundary line shown in Fig. 13b. The low stacking fault energy of IN718 superalloy facilitates the formation of deformation twins under conditions of high strain and high strain rate. Fig. 13c, d displays deformation twins in the plastic flow and transition layer, with bright-field (d1) and dark-field (d2) images of the same area showing deformation twin widths within the range of 60–70 nm, arranged in parallel. Fig. 14 shows the subsurface microstructure morphology of the workpiece ground at a speed of 240 m/s. As shown in Fig. 14a, compared to conventional grinding, the depth of the grain refinement layer decreases by 26 % to approximately 1.24 μm; the depth of the grain elongation layer is significantly reduced to about 1.94 μm, a reduction of nearly 63 %. It is worth noting that multifold nanoscale twins appear within the grains of the grain refinement layer, with twin widths ranging from 4 to 5 nm, as depicted in Fig. 14b, c. Due to the extremely high strain rate, these grains are more elongated than those observed at a conventional grinding speed of 40 m/s. Additionally, as illustrated in Fig. 14d, e, twins in the transition and plastic flow layers have widths of 16.88 nm and 61.83 nm, respectively. Notably, distinct multi-twin intersection structures are present in the plastic flow layer. The discovery of multi-twin intersection structures and multifold nano-twins shows that the strain rate effect is dominant under UHSM, and the plastic deformation form changes from dislocation movement to twin [28,29].

To further reveal the nanocrystalline grain information in the recrystallization layer at different grinding speeds, Fig. 15 shows IPF and grain orientation spread (GOS) images captured using the TKD technique. At grinding speeds of 40, 160, and 240 m/s, the average nanograin sizes are 62.8, 41.4, and 85.3 nm, respectively. Furthermore, Fig. 15d-f shows that compared with 40 m/s and 240 m/s, the color of recrystallized grains are simpler at 160 m/s, suggesting that the grain refinement is higher influenced by temperature effect and the new recrystallization grains undergo less plastic deformation [30]. Meanwhile, as grinding speed increases, the dominant hue changes from deep blue to light blue, and then to grass green. Especially, there is no absolute grain refinement layer at the speed of 240 m/s, as the grain misorientation intensifies. These phenomena indicate that a decrease in incubation time leads to increased incompleteness of recrystallization [31], with more energy transferred to the formation of nano-twins, suggesting that UHSM reduces the impact of temperature on subsurface material recrystallization. Meanwhile, increasing grain orientation is the typical feature of continuous dynamic recrystallization (cDRX). In addition, at a grinding speed of 40 m/s, lower intragranular misorientation and defects suggest that the recrystallization layer undergoes a more dynamic recovery process. It is worth pointing out that, compared the GOS of recrystallization layer at 160 m/s, large orientation grains are observed in recrystallization layers at both speeds of 40 m/s and 240 m/s, but the reasons are different. Large orientation grains at 40 m/s result from the plastic deformation of the recrystallization grains. While at 240 m/s, they are caused by the incomplete recrystallization.

Fig. 16 further summarizes the evolution of the microstructure within the grain refinement layer under different grinding speeds. In conventional machining, annealing twins and grain boundaries become optimal sites for dislocation nucleation, where dislocations move and accumulate to form dislocation cells and evolve further into new nanograins. Under a low strain rate condition, sufficient time is provided for grain growth and multiplication, allowing nanograins to further absorb surrounding dislocations, primarily through discontinuous

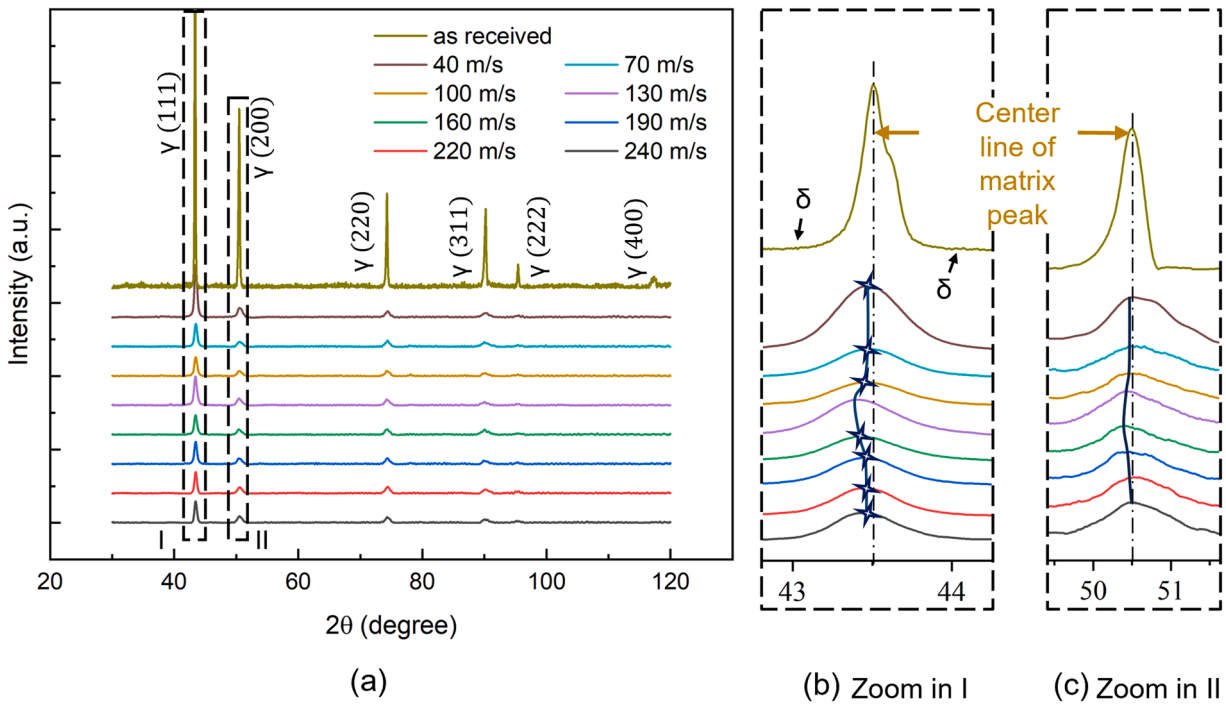

Fig. 7. XRD pattern of ground surface. (a) Diffraction peaks at different speeds; (b) and (c) represent enlarged views of regions I and II, respectively. It indicates that the surface plastic deformation increases first and then decreases with an increase in grinding speed.

dynamic recrystallization (dDRX) [32], eventually forming a grain refinement layer with low dislocation density, consistent with Fig. 12c. During high-speed machining, on one hand, the increased temperature influence intensifies grain refinement [33], while on the other, the increased strain rate inhibits further grain growth. Consequently, the dDRX grain nuclei does not have enough time to grow [34], and the process is dominated by cDRX and secondary dynamic recrystallization (sDRX), leading to smaller grains after recrystallization. When the grain size falls below a critical threshold, it becomes unfavorable for nano-twins formation. Under UHSM condition, the extremely high strain rate suppresses the effect of temperature, weakening recrystallization grain refinement. Meanwhile, the migration of large grain boundaries cannot be completed, and the process is predominantly governed by cDRX. The way of energy consumption changes into the formation of sub-grain boundaries and the incompleteness increases. Simultaneously, the dislocation movement is inhibited, and the recrystallization process cannot effectively offset all the energy imparted by UHSM, with part of the energy used for the nucleation of deformation twins, thus forming a nanocrystalline layer containing nano-twins, consistent with Fig. 14(b), (c).

3.5. Grinding temperature prediction

Due to the constraints of the grinding contact interface, directly measuring temperature in the grinding area is quite challenging. Particularly, during UHSM, the brief contact time between the wheel and the workpiece, coupled with ultra-high strain rate and ultra-rapid stress release, complicates accurate temperature measurement. Existing temperature measurement techniques, including contact types such as thermocouples and non-contact types such as thermography, suffer from low spatial resolution and slow response times, inadequately addressing the requirements for UHSM. Therefore, variations in grinding temperature can be deduced from trends in grinding forces and surface integrity.

During the ductile-mode removal in conventional grinding (20–70 m/s), increasing grinding speed intensifies plastic deformation, causing significant work hardening and increasing surface microhardness and grinding forces (Fig. 8). Simultaneously, intensified plastic deformation increases the heat generation, and under the influence of thermal stress, the depth of the subsurface damage layer within the workpiece gradually increases (Fig. 10a, b). Thus, during conventional grinding, grinding temperature rises with grinding speed increases. The density of the twins remains at a lower level under the effect of local heat accumulation [35], consistent with phenomena observed in Fig. 12.

During high-speed grinding (100–160 m/s), heat generation intensifies. Due to the temperature effects, material softening becomes evident, resulting in significant adhesion and side flow phenomena on the ground surface (as shown in Fig. 4f), and grinding forces gradually decrease. However, the increase in grinding speed shortens the contact time between the abrasive grains and the workpiece, leading to a reduced impact range of thermal stress and a decreased strain concentration area (as shown in Fig. 10c-e). Therefore, during high-speed grinding, the grinding temperature still rises and maintains at its peak, but the range of temperature impact for workpiece gradually decreases.

In ultra-high-speed grinding (220–240 m/s), the degree of plastic deformation is reduced, transitioning to the formation of nano-twins, thereby significantly suppressing the heat generated by internal friction. In addition, grinding forces remain stable compared to the speed range of 130–160 m/s. Still, as shown in Fig. 10, under ultra-high-speed grinding condition, the misorientation distribution of the workpiece subsurface is limited to the near-surface layer, indicating that the thermal effects are significantly localized. Consequently, during the ultra-high-speed grinding process, grinding temperature decreases, and its impact range for workpiece gradually reduces.

A similar temperature trend was observed in high-speed turning of aluminum alloy [36]. In the cutting speed range of 100–200 m/s, welded metal appeared on the tool's secondary cutting edge and side flow occurred on the finished surface, but disappeared when the cutting speed exceeded 200 m/s. The occurrence of welded metal indicates significant temperature effect at these machining speeds, accompanied by pronounced side flow on the surface of the machined material. Furthermore, in experiments involving ultra-high-speed turning of Ti-6Al-4V alloy [37], temperatures at the tool tip were successfully

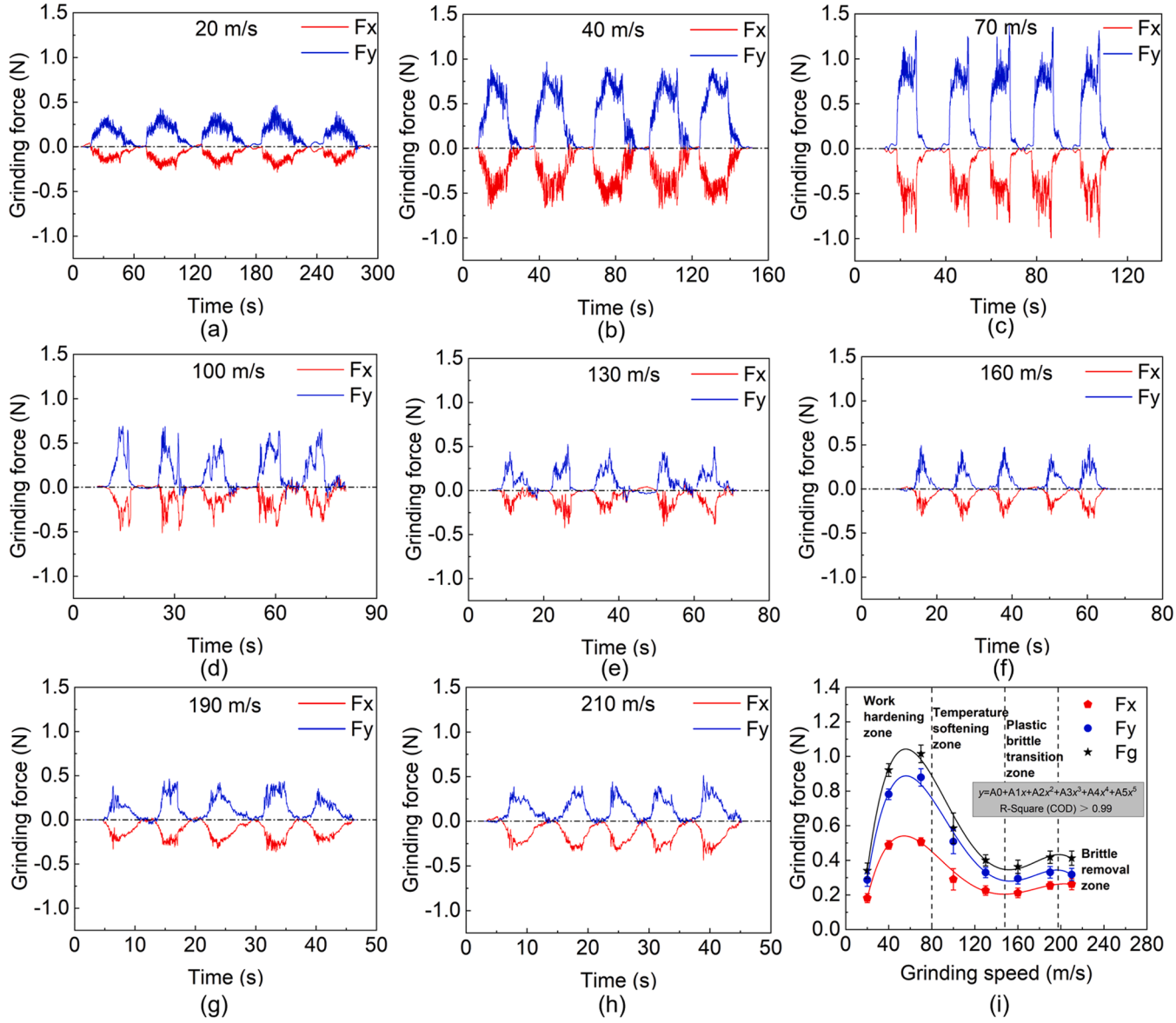

Fig. 8. Grinding force measurements at different grinding speeds (a) 20 m/s, (b) 40 m/s, (c) 70 m/s, (d) 100 m/s, (e) 130 m/s, (f) 160 m/s, (g) 190 m/s, (h) 210 m/s; and the variation trend of grinding force with grinding speed (i).

measured at different cutting speeds using the developed high-temperature transient thermometry system. Within a speed range of 7.5–212.6 m/s, the temperature first increased and then decreased, peaking at 1034°C at a cutting speed of 125.2 m/s.

4. Discussion

4.1. Material embrittlement mechanism in ultra-high-speed grinding and its influence on grinding force

Fig.s 9 and 10 demonstrate that beyond the grinding speed of 190 m/s, further increases in speed result in little change to subsurface. Both the altered layer dominated by mechanical stress and the misorientation concentration area caused by both mechanical and thermal stresses remain at the same level, indicating that the transition from ductile to brittle removal has completed and energy for material removal has reached a relative balance. The mode of material removal, either brittle or ductile, is visually evident in the morphology of the chips. To further verify this transition, scratching experiments were designed and conducted at the same machining depth (a_p=5 μm) but varying speeds, and the distance between adjacent scratches is 80 μm. The chips were collected for observation, as shown in Fig. 17. At the conventional speed range of 40–70 m/s, increasing scratching speed results in smaller chips, indicating that the strain rate effect dominates this speed range. When the speed increases to 100 m/s, the chip-breaking capability weakens, and large-sized serrated chips reemerge, indicating that temperature effect plays a major role as the material enters the high-speed range, with the material's plasticity enhanced by thermal softening. Further increasing the scratching speed, the chips evolve from serrated at 130 m/s to fragmented at 160 m/s, and ultimately to irregular chips at 190 m/s. The size of the chips significantly decreases, especially in the 160 m/s to 190 m/s range, where the overall size of the chips is less than one-tenth of that at conventional scratching speeds, and brittle penetrating cracks appeared inside the irregular chips at 190 m/s, indicating a gradual transition to the brittle-mode removal. It is worth pointing out that serrated chip formation is a process of adiabatic shear instability. And the transition from serrated chips to irregular chips indicates a change from discontinuous to continuous material removal.

Dislocation movement is widely used to reveal material deformation behavior, with dislocation slip being the primary movement mode as it

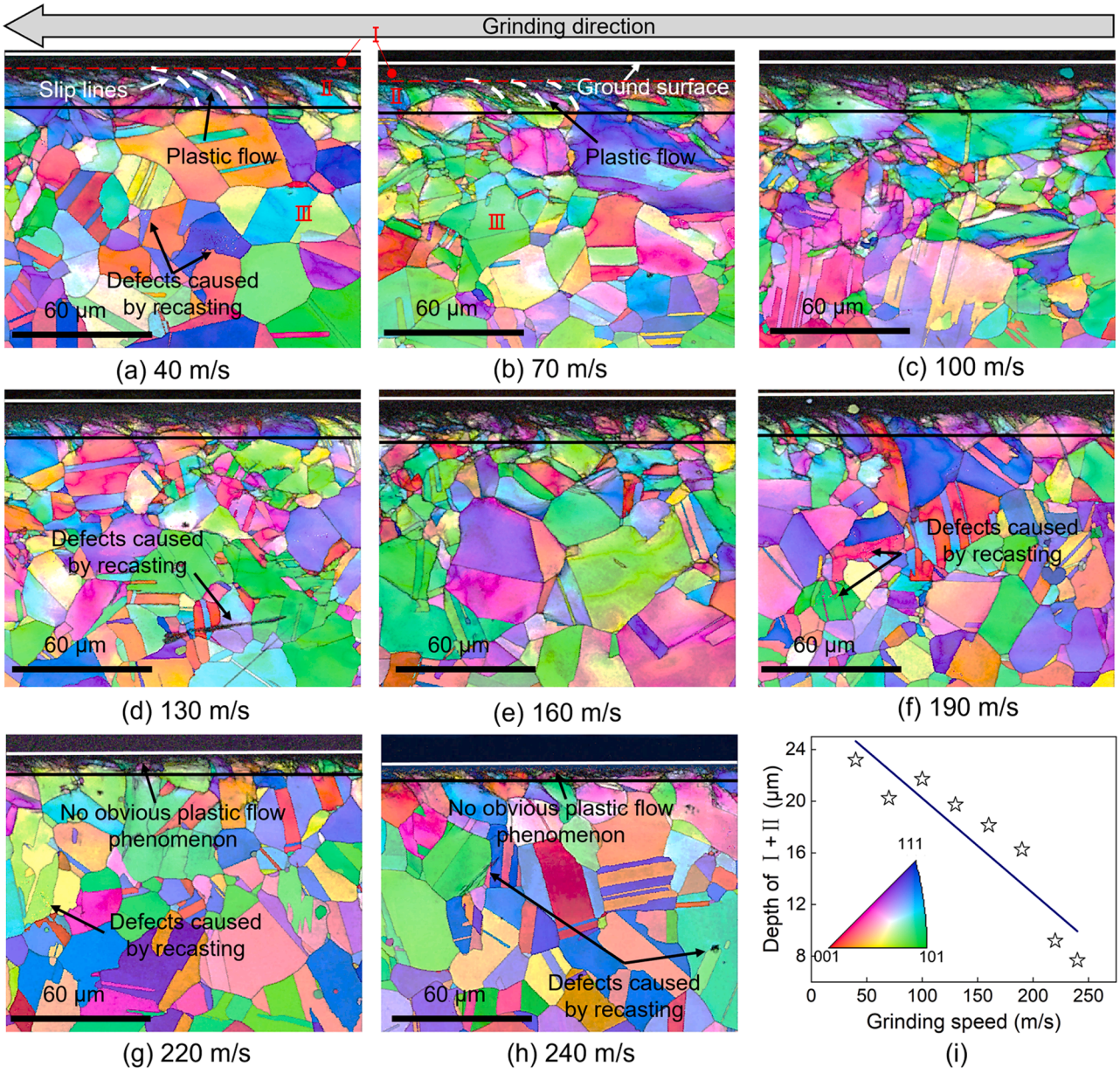

Fig. 9. Subsurface IPF+IQ at different grinding speeds (a) 40 m/s, (b) 70 m/s, (c) 100 m/s, (d) 130 m/s, (e) 160 m/s, (f) 190 m/s, (g) 220 m/s, (h) 240 m/s; and the variation trend of WPSD with grinding speed (i).

is easier to activate. According to dislocation movement theory, the higher the strain rate in conventional speed ranges, the faster the dislocation slip. To accommodate the increased speed of dislocation slip, atomic random vibrations intensify, making it hard to transfer energy effectively over longer distances within a short time. This results in significant local heating and the formation of adiabatic shear bands. Theoretically, an increase in machining speed raises the frequency of adiabatic shearing [38], generally enhancing chip-breaking capability. Notably, at high scratching speeds, particularly at 100 m/s, the temperature softening effect dominates, reducing the activation energy required for dislocation movement [39], thus revitalizing the material's plastic deformation coordination and weakening the chip-breaking ability, resulting in large-sized serrated chips. Of course, the speed of dislocation movement cannot increase indefinitely. At ultra-high strain rates, the energy dissipated by dislocation movement cannot offset the loaded energy, leading to massive multiplication of dislocations. Moreover, the driving force for dislocation movement changes from shear stress to hydrostatic pressure [40], thus dislocation movement shifts from an ordered (dislocation slip band form) to a disordered state [41]. Additionally, phonon drag plays a major role under ultra-high strain rate condition, and dislocation emission faces a larger energy barrier [42]. These factors lead to massive multiplication and entanglement of dislocations, gradually transitioning from mobile to immobile dislocations, ultimately causing dislocation avalanche, thereby entering the brittle-mode removal.

Dislocation movement directly determines the mechanical property of a material during its removal process. According to Orowan's dislocation bypass mechanism in classical fracture mechanics, the probability of successfully bypassing an obstacle during dislocation slip correlates directly with the obstacle's size. In the ductile-mode removal, the curvature radius R of the dislocation generated inside the workpiece and the applied shear stress τ exhibit the following relationship [43]:

$$R = \frac{Gb}{2\tau}\# \tag{1}$$

where G is the elastic modulus and b is the Burgers vector of the

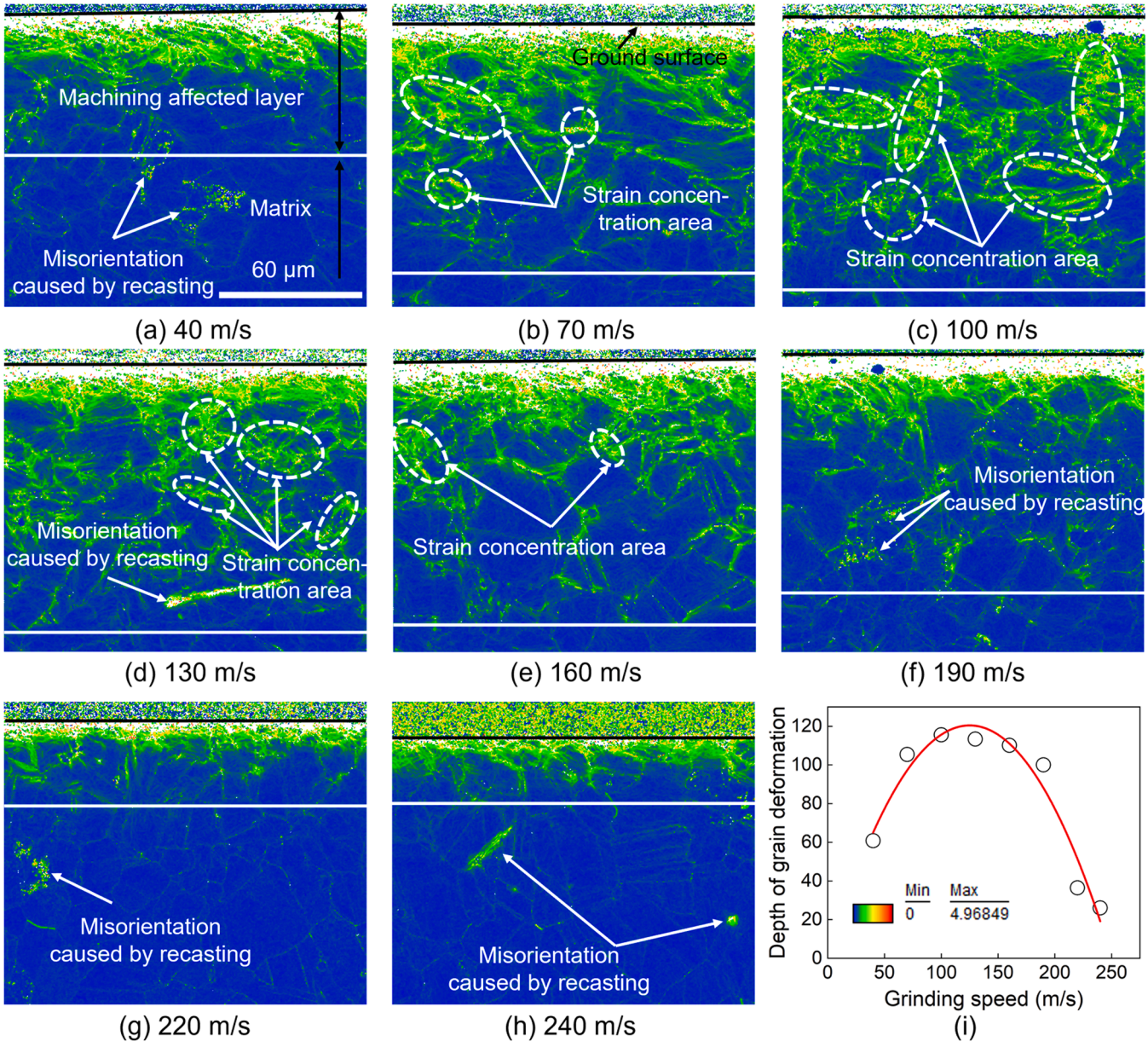

Fig. 10. Subsurface KAM at different grinding speeds (a) 40 m/s, (b) 70 m/s, (c) 100 m/s, (d) 130 m/s, (e) 160 m/s, (f) 190 m/s, (g) 220 m/s, (h) 240 m/s; and the variation trend of subsurface grain deformation layer depth with grinding speed (i).

workpiece material. Assuming the critical average distance between obstacles is D_{dn}, when $R = D_{dn}/2$, the dislocation can just bypass the obstacle, allowing the workpiece to undergo ductile-mode removal. Shear stress τ equals yield strength σ_s as in Eq. (2):

$$\sigma_s = \frac{Gb}{D_{dn}} \# \tag{2}$$

During the ductile-brittle transition of the material, the multiplication and entanglement of dislocations reduce the average distance between obstacles, preventing dislocations from passing through, thereby reducing fracture toughness and crack propagation resistance of the material. Meanwhile, according to Eq. (3), the surface energy γ_s decreases [9], and the grinding force decreases.

$$\sigma_a = \sqrt{\frac{(2E\gamma_s)}{\pi c}} \# \tag{3}$$

Here, σ_a represents the fracture toughness; E is the Young's modulus; and c is the length of existing cracks.

Of course, not all materials are suitable for UHSM. A prerequisite for UHSM is that the machining temperature must remain below the material's melting point before it gets embrittled. Therefore, high-melting-point and easily embrittled metal materials are more suitable for UHSM. Numerous factors affect the embrittlement of materials, notably crystal structure. The face-centered cubic structure, with its high symmetry and multiple slip systems, usually allows for more flexible dislocations. The body-centered cubic and hexagonal close-packed structures have relatively fewer slip systems, making the materials more prone to embrittlement. Additionally, internal microscopic defects, alloy elements and impurities also affect the movement of dislocations. For instance, impurity atoms may cause solid solution or precipitation strengthening, thereby inhibiting the movement of dislocations and making the material more susceptible to embrittlement. Together, these factors determine whether a material is suitable for UHSM.

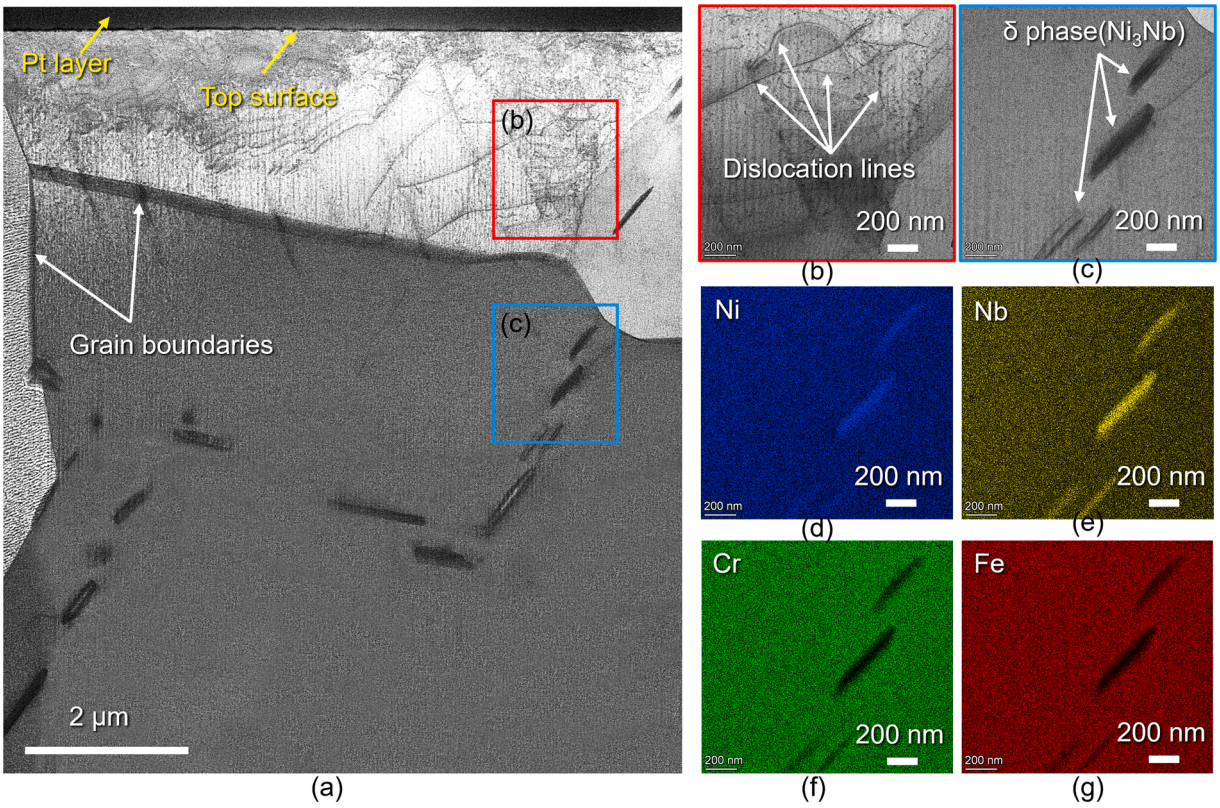

Fig. 11. Subsurface microstructure of an as-received sample. (a) Overall morphology; (b) and (c) are locally enlarged images of (a); (d), (e), (f), and (g) are EDS maps of (c).

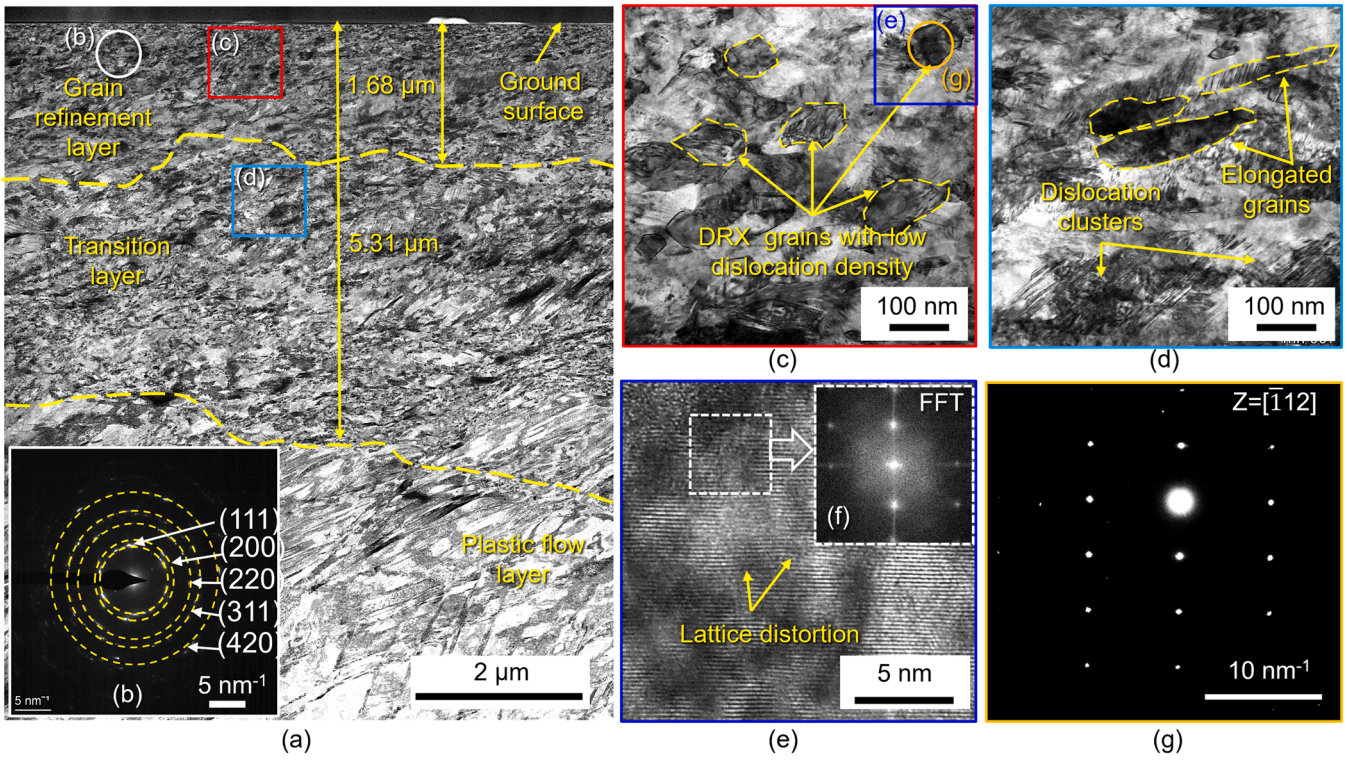

Fig. 12. Subsurface microstructure of ground workpiece at the speed of 40 m/s. (a) Overall morphology; (b) Electron diffraction pattern of the near-surface (white circle) region indicates recrystallized nanocrystals; (c) and (d) are locally enlarged images of (a), showing the microstructure of the grain refinement layer and transition layer, respectively; (e) is a local high-resolution magnification of (c), showing that there is only little lattice distortion; (f) is the local inverse Fourier transform; (g) is the selective electron diffraction of (c).

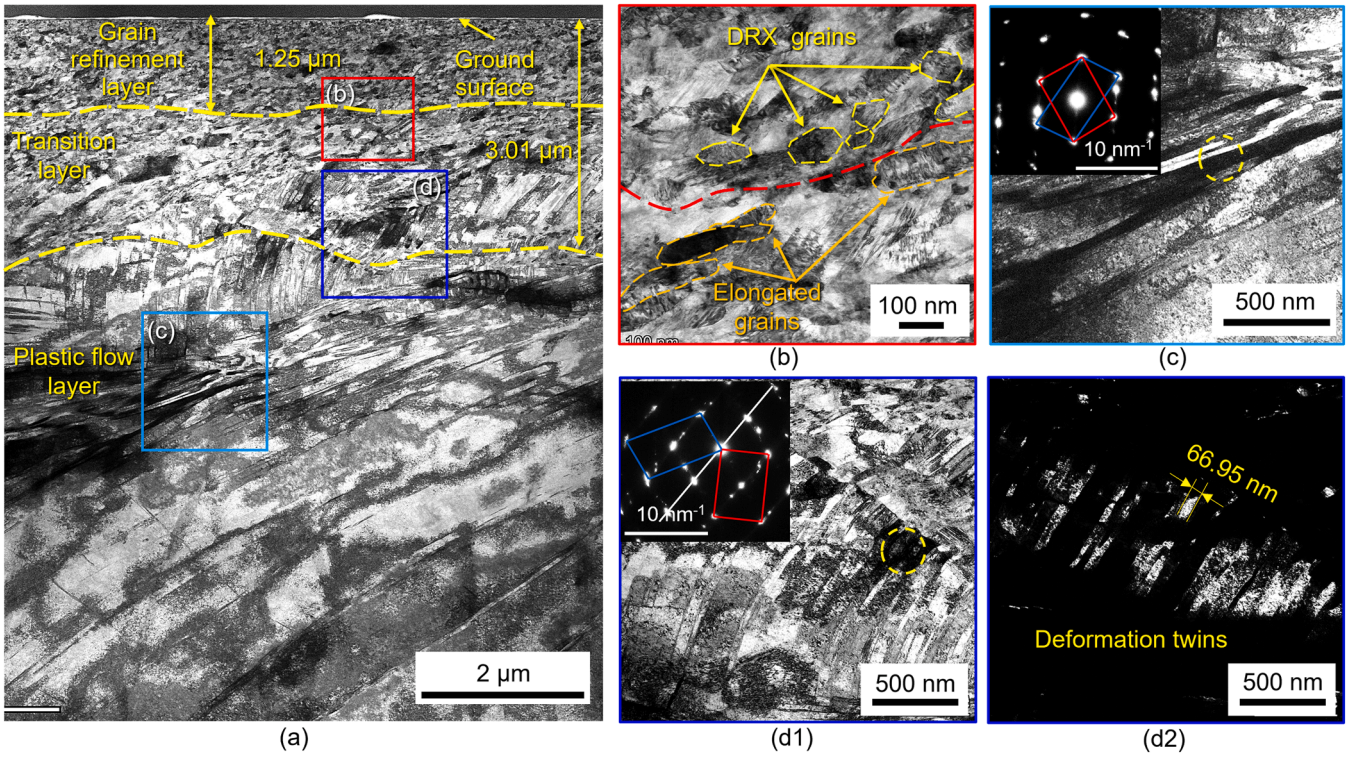

Fig. 13. Subsurface microstructure of ground workpiece at the speed of 160 m/s. (a) Overall morphology; (b), (c) and (d) are locally enlarged imagines of (a), in which the illustrations in (c) and (d1) show selected electron diffraction at the corresponding positions (yellow circle), and (d2) is the dark field map corresponding to (d1). It indicates that there are plenty of deformed twins in the transition and plastic flow layers.

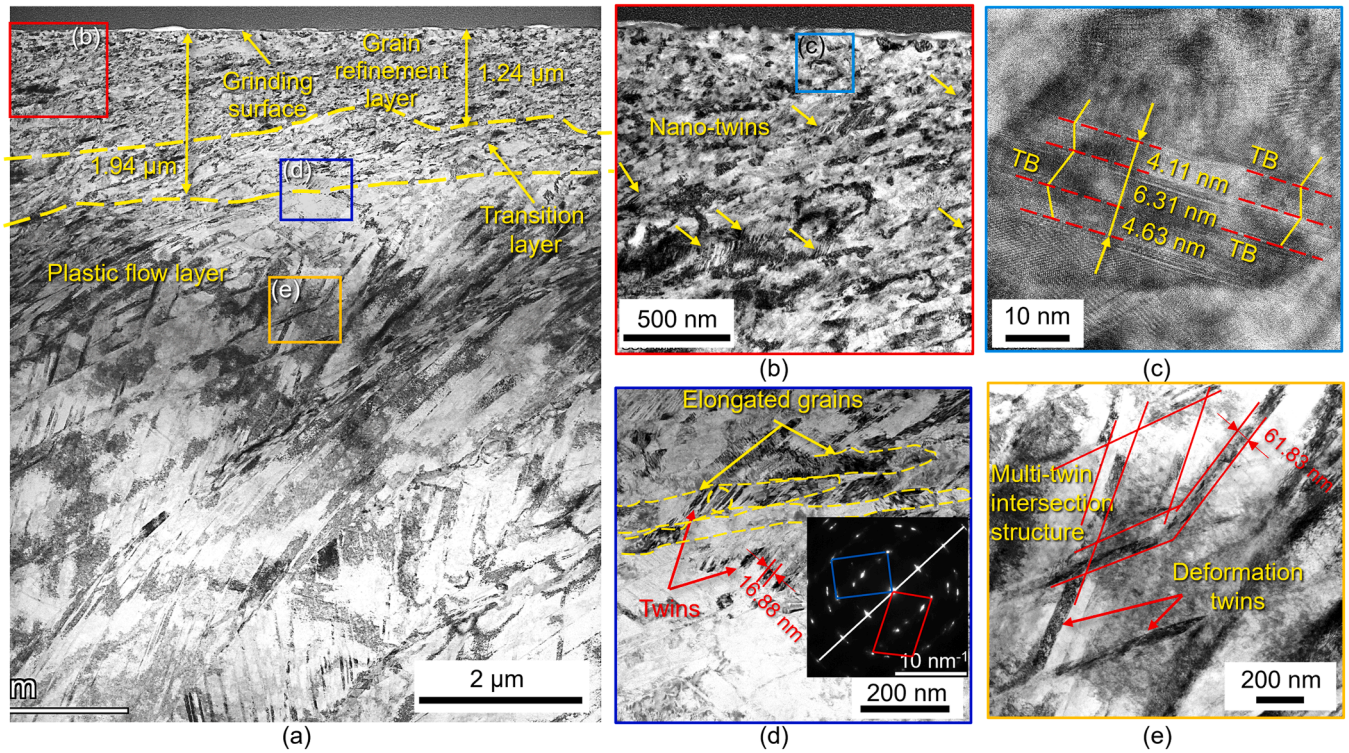

Fig. 14. Subsurface microstructure of ground workpiece at the speed of 240 m/s. (a) Overall morphology; (b), (d) and (e) are locally enlarged imagines of (a), in which the illustration in (d) shows selected electron diffraction at the corresponding position (yellow circle), and (c) is a local high-resolution magnification of (b), showing that there are multiple nanotwins in the grain refinement layer.

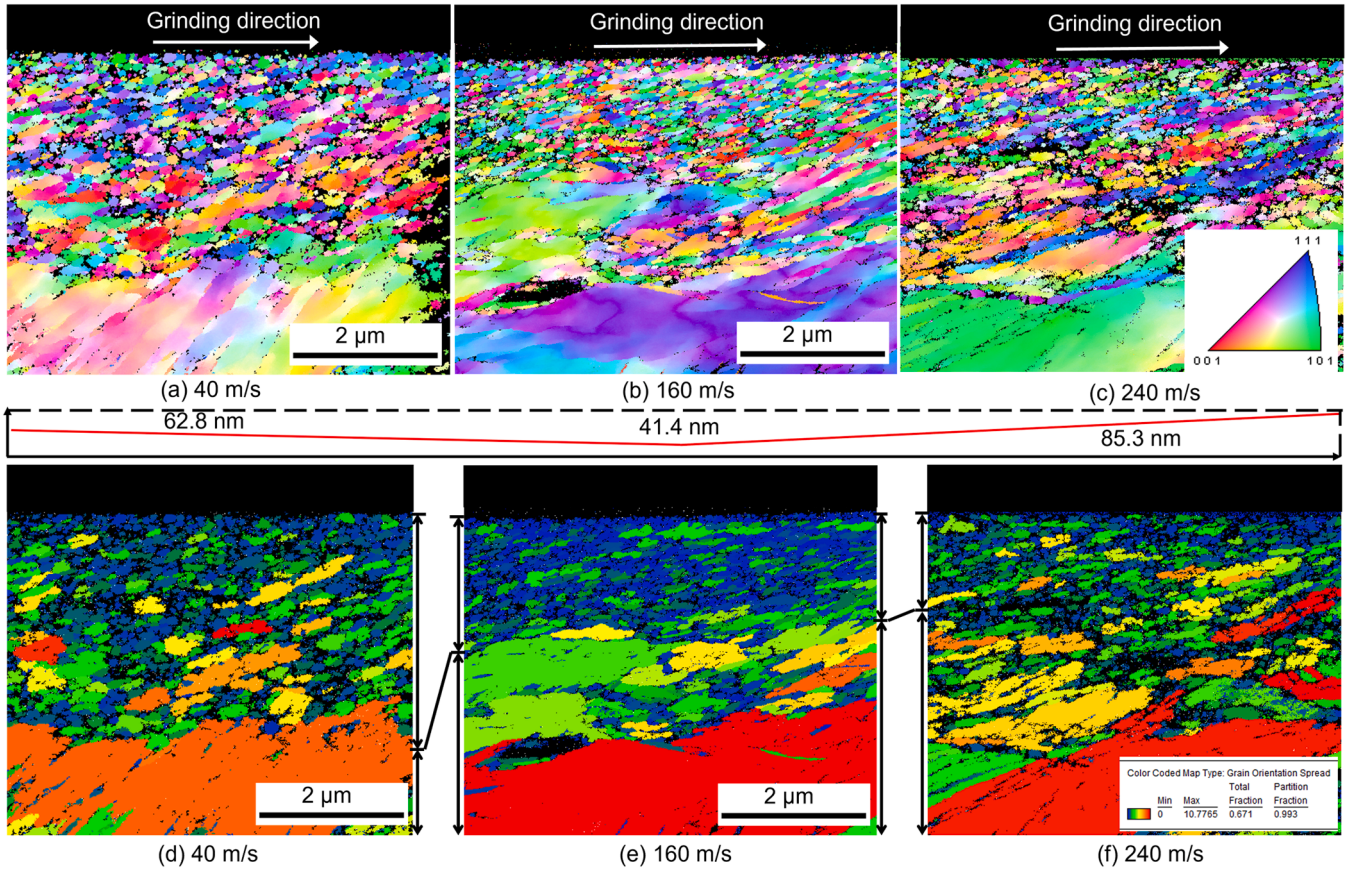

Fig. 15. TKD of ground workpiece. Subsurface IPF at different grinding speeds (a) 40 m/s, (b) 160 m/s, and (c) 240 m/s; Subsurface GOS at different grinding speeds (d) 40 m/s, (e) 160 m/s, and (f) 240 m/s, indicating that the GOS values increase first then decline with an increase in grinding speed. The middle red line indicates the variation of average grain size.

4.2. *Effect of material embrittlement on heat generation and transfer*

Material embrittlement in UHSM significantly alters heat generation and transfer [44]. As depicted in Fig. 18, in machining of metallic materials, approximately 75 %, 20 %, and 5 % of heat generation originates from internal friction in the primary deformation zone and external friction in the secondary and tertiary deformation zones, respectively. As the machining speed increases, chips gradually transition from continuous to serrated types, indicating intensified adiabatic shearing and increased heat generation in the primary deformation zone. Furthermore, with increased machining speeds, external friction in the secondary and tertiary deformation zones intensifies, resulting in severe heat generation and influence range. When entering UHSM, material embrittlement suppresses shear slip in the primary deformation zone, with energy primarily consumed in the form of molecular/atomic bond breaking, thereby significantly reducing heat from internal friction. Moreover, chips evolve from large serrated to small irregular fragmented types, significantly reducing their contact area with the tool and effectively diminishing heat from friction in the secondary deformation zone.

At ultra-high machining speeds, intense friction between the tool and the workpiece in the tertiary deformation zone significantly increases heat generation, which has become a new focal point in UHSM. Fortunately, in UHSM, the contact time between the tool and workpiece is extremely short, and the thermal conductivity of the workpiece material is further reduced under the influence of phonon drag at ultra-high strain rates [45], preventing deep penetration of heat generated in the tertiary deformation zone. Together, these factors promote the localization of thermal effect, confining microstructural change and stress-strain distribution to the shallow surface layer (as shown in Figs. 9 and 10). In addition, the brittle-mode removal in this paper specifically refers to chips leaving the workpiece surface via brittle fracture, and the surface still presents a ductile-mode removal feature after machining due to the influence of friction heat in the tertiary deformation zone, as shown in Fig. 4d. The above phenomenon may be caused by the different role of temperature on the strength of materials under different strain rates [46]. According to the calculation of Eq. (4) [18], the strain rate of the UHSM (above 190 m/s) is in the range of over 6.6×10^7 s^{-1}. At the extreme strain rate, the dislocation drag strengthening plays a more important role than the thermally controlled softening, so the metal's dynamic yield strength and dynamic hardness increase, and the chips are removed in a brittle mode. The strain rate decreases for the material under the tool, resulting in the thermal softening dominating, and the machined surface presents a ductile removal feature.

$$\frac{d\varepsilon}{dt} = \frac{\sqrt{3}V}{a_c}\# \tag{4}$$

where V represents the machining speed, and a_c is the machining depth.

4.3. *Machinability at different grinding speeds*

Low thermal conductivity, severe work hardening, and significant tool wear due to hard phases are major challenges in machining IN718 superalloy. Given the randomness of hard phases, this section primarily discusses the first two factors and surface integrity. As shown in Fig. 19, grinding force and surface roughness are the main factors affecting machinability in conventional machining. On one hand, intensified plastic deformation results in severe work hardening, sharply increasing the grinding force as speed increases. On the other hand, at a low

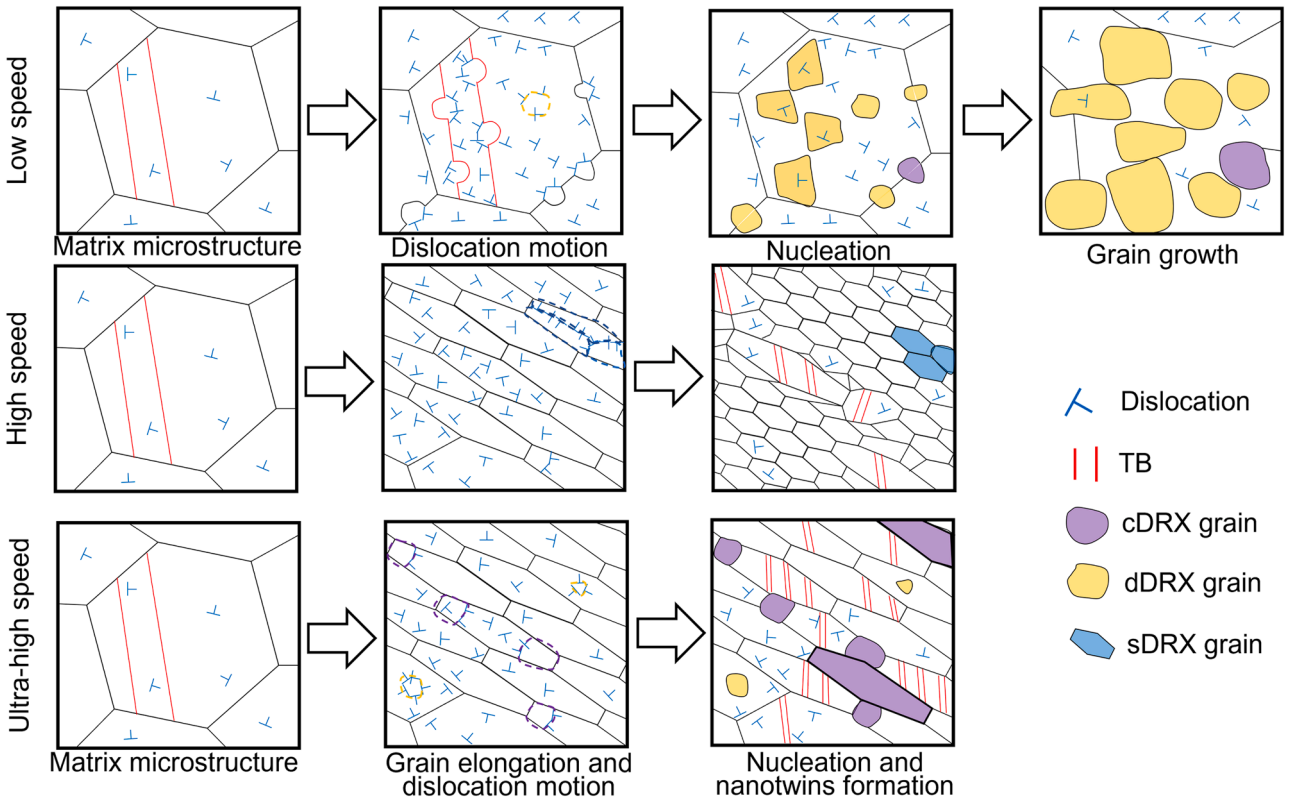

Fig. 16. Schematic diagram of recrystallization evolution of grain refinement layer at different grinding speeds.

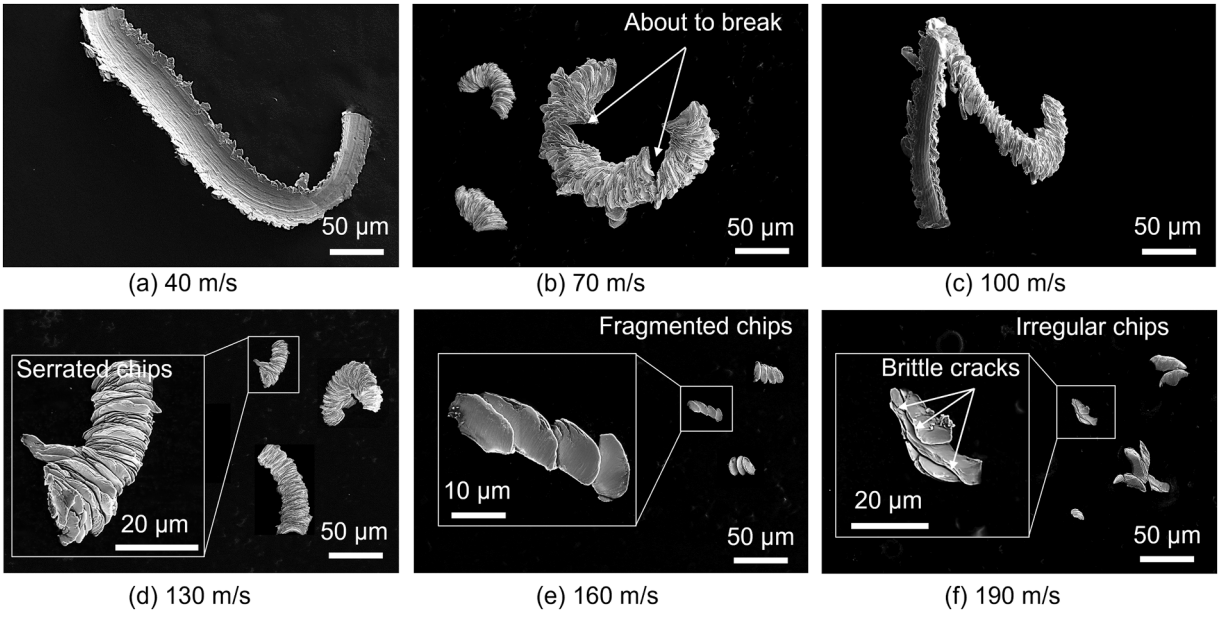

Fig. 17. Chip morphology at different scratching speeds. (a) 40 m/s, (b) 70 m/s, (c) 100 m/s, (d) 130 m/s, (e) 160 m/s, and (f) 190 m/s.

machining speed, the removed material tends to coat the machined surface, resulting in the worst surface roughness. In high-speed machining, the reduction in grinding force is attributed to thermal softening and decreased undeformed chip thickness. However, this brings a new machining challenge: an increased range of subsurface damage due to thermal stress. Simultaneously, thermal softening causes severe lattice distortion on the surface, further exacerbating plastic deformation, reaching the maximum surface microhardness after machining (100 m/s and 130 m/s). Of course, with the increased speed in the high-speed machining range, the size and amount of material smearing on the machined surface are further reduced, and the surface roughness is further optimized. Consequently, reduced grinding force and improved surface finish are the main advantages of high-speed machining, while the unavoidable thermal effect becomes the primary factor limiting the machinability of IN718 superalloy within this speed range.

In the order of increasing machining speed/energy, metal response is classified into elastic deformation, plastic deformation, and brittle

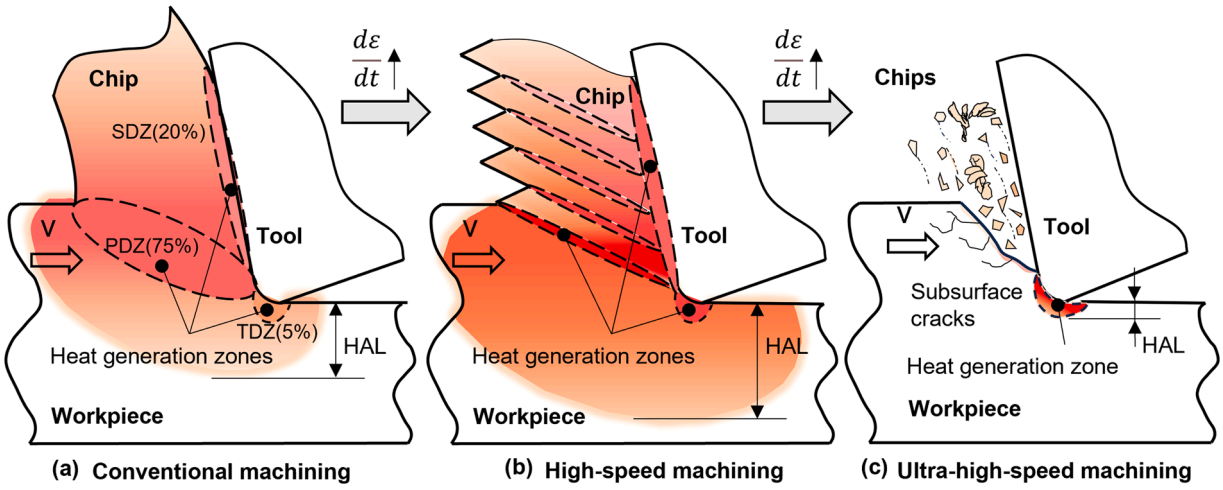

Fig. 18. Effect of machining speed on heat generation and distribution. (a) Conventional machining; (b) High-speed machining; (c) Ultra-high-speed machining.

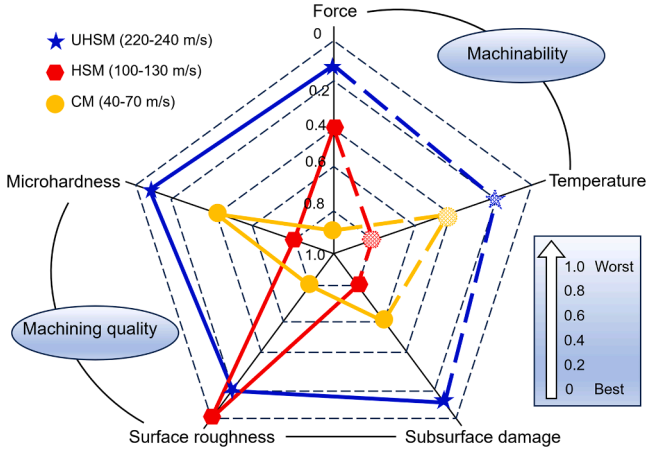

Fig. 19. Machinability of IN718 superalloy at different machining speed ranges.

fracture, each associated with further reduced machining resistance of the workpiece material. As machining speed increases, the time available for plastic deformation decreases, concurrently reducing machining energy consumption [47]. In UHSM, plastic deformation of the workpiece is significantly suppressed, making brittle fracture the dominant mode of material removal. Consequently, this leads to further reductions in grinding force and minimal surface microhardness, effectively addressing the problem of severe work hardening in the IN718 superalloy. Moreover, reducing plastic deformation significantly lowers heat generation, and the extremely short contact time between the tool and the workpiece further restricts heat transfer deep into the workpiece, localizing subsurface damage to the shallow layers and presenting the skin effect of machining damage. The elimination of thermal effects effectively prevents the formation of inferior Laves phases caused by high-temperature-induced Nb segregation, maintaining the material's original strength and resistance to fatigue and creep, and reducing the consumption of elements needed for precipitation strengthening, thus effectively inhibiting crack initiation and propagation [48]. Furthermore, from the perspective of the subsurface microstructure, compared to the low-density dislocation recrystallization layer in conventional machining, UHSM under high-energy impact produces a nanocrystalline layer with nano-twin structures, improving the mechanical property of IN718 superalloy components. Meanwhile, the recrystallization layer decreases under the UHSM condition, increasing the fatigue life [49]. Thus, UHSM addresses the challenges of both low thermal conductivity and severe work hardening, achieving high-quality and high-efficiency, which is crucial for difficult-to-machine materials such as IN718 superalloy.

5. Conclusions

This paper first achieved ultra-high-speed grinding of IN718 superalloy up to 240 m/s, thoroughly explored the formation mechanism of the ground surface, and revealed the machinability of IN718 superalloy at different grinding speeds. The conclusions are summarized as follows:

(1) Ultra-high-speed machining (UHSM) can achieve brittle-mode removal of ductile materials, and different materials correspond to different critical machining speeds. In micron-level precision grinding, the critical speed of IN718 superalloy is 190 m/s. Beyond this speed, the depth of subsurface damage tends to stabilize and remains at a minimum level. Simultaneously, the size of the chips drastically reduces, with penetrating cracks, exhibiting characteristics of brittle-mode removal and entering UHSM.

(2) Higher grinding speeds result in improved surface quality, primarily due to reduced size and level of material smearing, and a decrease in the undeformed chip thickness, leading to shallower grinding marks.

(3) Strain, strain rate, and temperature are the main factors affecting the material removal mechanism. Different grinding speed intervals correspond to different dominant factors. In the conventional grinding range, significant work hardening occurs, resulting in the highest grinding force. Meanwhile, subsurface plastic flow is pronounced, and the WPSD is up to 24 μm. In the high-speed grinding range, thermal softening is predominant, resulting in optimal surface quality and a reduced WPSD. However, the range of thermal effects is extensive, particularly at the onset of high-speed grinding (100 m/s, 120 μm). Under ultra-high-speed grinding condition, strain rate dominates and brittle-mode removal of plastic material occurs, with both the WPSD and thermal affected layer confined to the minimum range. Concurrently, the ground surface retains characteristics of ductile-mode removal, with no significant cracks observed.

(4) For metal materials, the grinding speed affects the grain refinement mechanism of recrystallized layer. In conventional grinding, severe plastic deformation, notable thermal effect and adequate time mainly promote dDRX. However, during ultra-high-speed grinding, the thermal effect is weakened, and plastic deformation is significantly suppressed, favoring cDRX.

Meanwhile, the ultra-high-speed impact results in the formation of multifold nano-twins.

(5) The essence of plastic deformation in the grain refinement layer, transitioning from dislocation movement to nano-twins formation, lies in the increase of recrystallization incompleteness. UHSM can improve the recrystallization incompleteness of IN718 superalloy, leading to the generation of multifold nanotwins.

(6) Ultra-high-speed grinding can simultaneously address the two significant challenges of low thermal conductivity and severe work hardening in IN718 superalloy. Its minimal subsurface damage depth significantly reduces the time required for subsequent polishing, facilitating the rapid production of high-quality, undamaged machined parts. This provides a new approach to improving the machinability of difficult-to-machine materials.

CRediT authorship contribution statement

Bi Zhang: Conceptualization, Funding acquisition, Project administration, Supervision, Writing – review & editing. **Qinghong Jiang:** Formal analysis, Investigation, Methodology. **Hao Liu:** Conceptualization, Formal analysis, Investigation, Methodology, Writing – original draft, Writing – review & editing. **Huili Han:** Methodology, Writing – review & editing.

Declaration of Competing Interest

The authors declare that they have no known competing financial interests or personal relationships that could have appeared to influence the work reported in this paper.

Acknowledgements

This work was supported by Shenzhen Science and Technology Innovation Commission (grant nos. KQTD20190929172505711, GJHZ20210705141807023, JCYJ20210324115413036, and JSGG20220831110605009), Guangdong Basic and Applied Basic Research Foundation (2021B1515120009) and High level of special funds (G03034K003, 2019JC01Z031) from Southern University of Science and Technology. The authors acknowledge the assistance of SUSTech Core Research Facilities.

References

[1] la Monaca, A., Liao, Z., Axinte, D.A., M'Saoubi, R., Hardy, M.C., 2022. Can higher cutting speeds and temperatures improve the microstructural surface integrity of advanced Ni-base superalloys? CIRP Ann. 71, 113–116. https://doi.org/10.1016/j.cirp.2022.04.061.

[2] Liu, H., Han, H., Jiang, Q., He, M., Zhang, B., 2024. Characterization and analysis of inconel 718 alloy ground at different speeds. Chin. J. Mech. Eng. 37, 34. https://doi.org/10.1186/s10033-024-01017-5.

[3] Sarıkaya, M., Gupta, M.K., Tomaz, I., Pimenov, D.Y., Kuntoğlu, M., Khanna, N., Yıldırım, Ç.V., Krolczyk, G.M., 2021. A state-of-the-art review on tool wear and surface integrity characteristics in machining of superalloys. CIRP J. Manuf. Sci. Tech. 35, 624–658. https://doi.org/10.1016/j.cirpj.2021.08.005.

[4] Aramcharoen, A., Chuan, S.K., 2014. An experimental investigation on cryogenic milling of inconel 718 and its sustainability assessment. Procedia CIRP 14, 529–534. https://doi.org/10.1016/j.procir.2014.03.076.

[5] Musfirah, A.H., Ghani, J.A., Haron, C.H.C., 2017. Tool wear and surface integrity of inconel 718 in dry and cryogenic coolant at high cutting speed. Wear 376-377, 125–133. https://doi.org/10.1016/j.wear.2017.01.031.

[6] Shah, P., Bhat, P., Khanna, N., 2021. Life cycle assessment of drilling Inconel 718 using cryogenic cutting fluids while considering sustainability parameters. Sustain. Energy Techn. 43, 100950. https://doi.org/10.1016/j.seta.2020.100950.

[7] Courbon, C., Sajn, V., Kramar, D., Rech, J., Kosel, F., Kopac, J., 2011. Investigation of machining performance in high pressure jet assisted turning of Inconel 718: a numerical model. J. Mater. Process. Technol. 211, 1834–1851. https://doi.org/10.1016/j.jmatprotec.2011.06.006.

[8] Courbon, C., Kramar, D., Krajnik, P., Pusavec, F., Rech, J., Kopac, J., 2009. Investigation of machining performance in high-pressure jet assisted turning of Inconel 718: an experimental study. Int. J. Mach. Tools Manuf. 49, 1114–1125. https://doi.org/10.1016/j.ijmachtools.2009.07.010.

[9] Yin, Q., Liu, Z., Wang, B., 2021. Machinability improvement of Inconel 718 through mechanochemical and heat transfer effects of coated surface-active thermal conductive mediums. J. Alloy. Compd. 876, 160186. https://doi.org/10.1016/j.jallcom.2021.160186.

[10] Bermingham, M.J., Kirsch, J., Sun, S., Palanisamy, S., Dargusch, M.S., 2011. New observations on tool life, cutting forces and chip morphology in cryogenic machining Ti-6Al-4V. Int. J. Mach. Tools Manuf. 51, 500–511. https://doi.org/10.1016/j.ijmachtools.2011.02.009.

[11] Krajnik, P., Rashid, A., Pušavec, F., Remškar, M., Yui, A., Nikkam, N., Toprak, M.S., 2016. Transitioning to sustainable production – part III: developments and possibilities for integration of nanotechnology into material processing technologies. J. Clean. Prod. 112, 1156–1164. https://doi.org/10.1016/j.jclepro.2015.08.064.

[12] Haq, M.Au, Hussain, S., Ali, M.A., Farooq, M.U., Mufti, N.A., Pruncu, C.I., Wasim, A., 2021. Evaluating the effects of nano-fluids based MQL milling of IN718 associated to sustainable productions. J. Clean. Prod. 310, 127463. https://doi.org/10.1016/j.jclepro.2021.127463.

[13] Garcí, a Navas, V., Arriola, I., Gonzalo, O., Leunda, J., 2013. Mechanisms involved in the improvement of Inconel 718 machinability by laser assisted machining (LAM). Int. J. Mach. Tools Manuf. 74, 19–28. https://doi.org/10.1016/j.ijmachtools.2013.06.009.

[14] Moon, S.-H., Lee, C.-M., 2018. A study on the machining characteristics using plasma assisted machining of AISI 1045 steel and Inconel 718. Int. J. Mech. Sci. 142-143, 595–602. https://doi.org/10.1016/j.ijmecsci.2018.05.020.

[15] Yang, X., Zhang, B., 2019. Material embrittlement in high strain-rate loading. Int. J. Extrem. Manuf. 1, 022003. https://doi.org/10.1088/2631-7990/ab263f.

[16] Zhang, B., Yin, J., 2019. The 'skin effect' of subsurface damage distribution in materials subjected to high-speed machining. Int. J. Extrem. Manuf. 1, 012007. https://doi.org/10.1088/2631-7990/ab103b.

[17] Eda, H., Kishi, K., Hashimoto, H., 1981. Surface generation by super high speed cutting up to 1200m/s. In: Alexander, J.M. (Ed.), Proceedings of the Twenty-First International Machine Tool Design and Research Conference. Macmillan Education UK, Palgrave, London, pp. 259–265. https://doi.org/10.1007/978-1-349-05861-7_34.

[18] Wang, B., Liu, Z., 2016. Investigations on deformation and fracture behavior of workpiece material during high speed machining of 7050-T7451 aluminum alloy. CIRP J. Manuf. Sci. Tech. 14, 43–54. https://doi.org/10.1016/j.cirpj.2016.05.007.

[19] Zhou, L., Shimizu, J., Muroya, A., Eda, H., 2003. Material removal mechanism beyond plastic wave propagation rate. Precis. Eng. 27, 109–116. https://doi.org/10.1016/s0141-6359(02)00124-1.

[20] Liu, Z., Su, G., 2012. Characteristics of chip evolution with elevating cutting speed from low to very high, 54-55 Int. J. Mach. Tools Manuf. 82–85. https://doi.org/10.1016/j.ijmachtools.2011.12.003.

[21] Wang, B., Liu, Z., Su, G., Ai, X., 2015. Brittle removal mechanism of ductile materials with ultrahigh-speed machining. J. Manuf. Sci. E. -T. ASME 137, 061002. https://doi.org/10.1115/1.4030826.

[22] Guo, S., Lu, S., Zhang, B., Cheung, C.F., 2022. Surface integrity and material removal mechanisms in high-speed grinding of Al/SiCp metal matrix composites. Int. J. Mach. Tools Manuf. 178, 103906. https://doi.org/10.1016/j.ijmachtools.2022.103906.

[23] Jiang, Q., Li, S., Liu, H., Fu, M., Zhang, B., 2024. Material removal mechanisms in ultra-high-speed scratching of Ti6Al4V alloy by selective laser melting. J. Manuf. Process. 127, 645–659. https://doi.org/10.1016/j.jmapro.2024.07.145.

[24] Ueda, Y., Sakurai, N., Takagi, T., Ishizu, K., Yan, J., 2022. Exploratory investigation of chip formation and surface integrity in ultra-high-speed gear hobbing. CIRP Ann. 71, 89–92. https://doi.org/10.1016/j.cirp.2022.03.030.

[25] Korneeva, V.M., Korneev, S.S., 2021. Implementation of ultra-high speed machining with an edge tool. AIP Conf. Proc. 2318, 150001. https://doi.org/10.1063/5.0036374.

[26] Zhang, Y., Li, C., Jia, D., Zhang, D., Zhang, X., 2015. Experimental evaluation of the lubrication performance of MoS2/CNT nanofluid for minimal quantity lubrication in Ni-based alloy grinding. Int. J. Mach. Tools Manuf. 99, 19–33. https://doi.org/10.1016/j.ijmachtools.2015.09.003.

[27] Liao, Z., Polyakov, M., Diaz, O.G., Axinte, D., Mohanty, G., Maeder, X., Michler, J., Hardy, M., 2019. Grain refinement mechanism of nickel-based superalloy by severe plastic deformation - Mechanical machining case. Acta Mater. 180, 2–14. https://doi.org/10.1016/j.actamat.2019.08.059.

[28] Voisin, T., Grapes, M.D., Li, T.T., Santala, M.K., Zhang, Y., Ligda, J.P., Lorenzo, N. J., Schuster, B.E., Campbell, G.H., Weihs, T.P., 2020. In situ TEM observations of high-strain-rate deformation and fracture in pure copper. Mater. Today 33, 10–16. https://doi.org/10.1016/j.mattod.2019.11.001.

[29] Bringa, E.M., Caro, A., Wang, Y., Victoria, M., McNaney, J.M., Remington, B.A., Smith, R.F., 2005. Ultrahigh strength innanocrystalline materials under shock loading. Science 309, 1838–1841. https://doi.org/10.1126/science.1116723.

[30] Zhou, X., He, L., Zhou, T., Jiang, H., Xu, J., Tian, P., Zou, Z., Du, F., 2022. Multiscale research of microstructure evolution during turning Ti-6Al-4V alloy based on FE and CA. J. Alloy. Compd. 922, 166202. https://doi.org/10.1016/j.jallcom.2022.166202.

[31] Ding, S., Taylor, T., Khan, S.A., Sato, Y., Yanagimoto, J., 2022. Further understanding of metadynamic recrystallization through thermomechanical tests and EBSD characterization. J. Mater. Process. Technol. 299, 117359. https://doi.org/10.1016/j.jmatprotec.2021.117359.

[32] Wei, S., Zhang, H., Tangpatjaroen, C., Tarnsangpradit, J., Usta, A.D., Eriten, M., Perepezko, J.H., Szlufarska, I., 2021. Wear-induced microstructural evolution of ultra-fine grained (UFGs) aluminum. Acta Mater. 209, 116787. https://doi.org/10.1016/j.actamat.2021.116787.

[33] Jia, D., Sun, W., Xu, D., Liu, F., 2019. Dynamic recrystallization behavior of GH4169G alloy during hot compressive deformation. J. Mater. Sci. Technol. 35, 1851–1859. https://doi.org/10.1016/j.jmst.2019.04.018.
[34] Zhao, W., Liu, H., Outeiro, J., Xu, X., Zhang, J., 2020. Simulation of grain refinement induced by high-speed machining of OFHC copper using cellular automata method. J. Manuf. Sci. E. -T. ASME 142, 091006. https://doi.org/10.1115/1.4047431.
[35] Li, B., Liu, H., Zhang, J., Xu, B., Zhao, W., 2023. Multi-mechanism-based twinning evolution in machined surface induced by thermal-mechanical loads with increasing cutting speeds. Int. J. Mach. Tools Manuf. 192, 104074. https://doi.org/10.1016/j.ijmachtools.2023.104074.
[36] Yousefi, R., Ichida, Y., 2000. A study on ultra–high-speed cutting of aluminium alloy: formation of welded metal on the secondary cutting edge of the tool and its effects on the quality of finished surface. Precis. Eng. 24, 371–376. https://doi.org/10.1016/S0141-6359(00)00048-9.
[37] Su, M.-Y., Wang, D.-R., Wang, Q., Jiang, M.-Q., Dai, L.-H., 2023. Towards Salomon's hypothesis via ultra-high-speed cutting Ti-6Al-4V alloy. Int. J. Adv. Manuf. Technol. 129, 5679–5690. https://doi.org/10.1007/s00170-023-12668-4.
[38] Ye, G.G., Xue, S.F., Ma, W., Jiang, M.Q., Ling, Z., Tong, X.H., Dai, L.H., 2012. Cutting AISI 1045 steel at very high speeds. Int. J. Mach. Tools Manuf. 56, 1–9. https://doi.org/10.1016/j.ijmachtools.2011.12.009.
[39] Meyers, M.A., Benson, D.J., Vöhringer, O., Kad, B.K., Xue, Q., Fu, H.-H., 2002. Constitutive description of dynamic deformation: physically-based mechanisms. Mater. Sci. Eng. A 322, 194–216. https://doi.org/10.1016/S0921-5093(01)01131-5.
[40] Zhang, J., He, B., Zhang, B., 2023. Failure mode change and material damage with varied machining speeds: a review. Int. J. Extrem. Manuf. 5, 022003. https://doi.org/10.1088/2631-7990/acbd6f.
[41] Meng, B., Yuan, D., Xu, S., 2019. Study on strain rate and heat effect on the removal mechanism of SiC during nano-scratching process by molecular dynamics simulation. Int. J. Mech. Sci. 151, 724–732. https://doi.org/10.1016/j.ijmecsci.2018.12.022.
[42] Gurrutxaga-Lerma, B., Balint, D.S., Dini, D., Sutton, A.P., 2015. The mechanisms governing the activation of dislocation sources in aluminum at different strain rates. J. Mech. Phys. Solids 84, 273–292. https://doi.org/10.1016/j.jmps.2015.08.008.
[43] Wang, R., Zhao, M., Mao, J., Liang, S.Y., 2022. Force prediction and material removal mechanism analysis of milling SiCp/2009Al. Micromachines 13, 1687. https://doi.org/10.3390/mi13101687.
[44] Su, G., Xiao, X., Du, J., Zhang, J., Zhang, P., Liu, Z., Xu, C., 2020. On cutting temperatures in high and ultrahigh-speed machining. Int. J. Adv. Manuf. Technol. 107, 73–83. https://doi.org/10.1007/s00170-020-05054-x.
[45] Ali, Y.M., Zhang, L.C., 2005. Relativistic heat conduction. Int. J. Heat. Mass Tran. 48, 2397–2406. https://doi.org/10.1016/j.ijheatmasstransfer.2005.02.003.
[46] Dowding, I., Schuh, C.A., 2024. Metals strengthen with increasing temperature at extreme strain rates. Nature 630, 91–95. https://doi.org/10.1038/s41586-024-07420-1.
[47] Wang, B., Liu, Z., Song, Q., Wan, Y., Ren, X., 2019. An approach for reducing cutting energy consumption with ultra-high speed machining of super alloy Inconel 718. Int. J. Pr. Eng. Man. -G. T. 7, 35–51. https://doi.org/10.1007/s40684-019-00125-1.
[48] Yin, Q., Liu, Z., Wang, B., Song, Q., Cai, Y., 2020. Recent progress of machinability and surface integrity for mechanical machining Inconel 718: a review. Int. J. Adv. Manuf. Technol. 109, 215–245. https://doi.org/10.1007/s00170-020-05665-4.
[49] Herbert, C., Axinte, D.A., Hardy, M., Withers, P., 2014. Influence of surface anomalies following hole making operations on the fatigue performance for a nickel-based superalloy. J. Manuf. Sci. E. T. ASME 136, 051016. https://doi.org/10.1115/1.4027619.